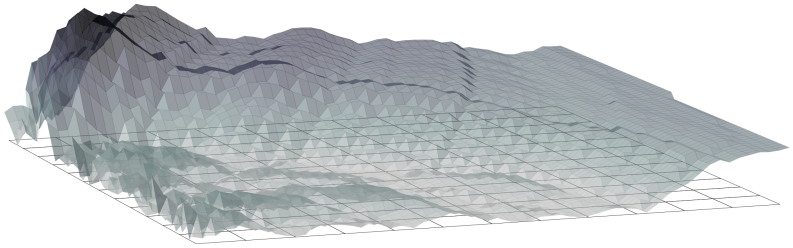

Ludwig-Maximilians-Universität

Master Thesis

Phase Walk Analysis for Leptokurtic Time Series

Author:
Korbinian Schreiber

Supervisors:
Prof. Dr. Gregor Morfill
Dr. Christoph Räth

Munich, September 29, 2015

The cover art is a three-dimensional representation of phase walk analysis results for a time series with low-frequency nonlinearities. It corresponds to Fig. 4.5D and is explained in Section 4.5.

Ludwig-Maximilians-Universität

Masterarbeit

Analyse der Fourier Phasen leptokurtischer Zeitserien

Autor:
Korbinian Schreiber

Betreuer:
Prof. Dr. Gregor Morfill
Dr. Christoph Räth

München, den 29. September 2015

Contents

Chapter 1

Introduction

Modern time series analysis offers a great variety of measures to characterize and quantify chaos and / or nonlinearities. The bandwidth of applications is immense, stretching from physiology[1] or epidemiology[2] over physics[3] to finance and economics[4]. With the help of nonlinear diagnosis, it became possible to detect or to even forecast life threatening diseases[5], stock market behavior[6] or rogue events in ocean waves or photonic media[7].

The most celebrated tools in the field are typically borrowed from dynamical systems- [Kantz, 1994; Sugihara and May, 1990] or fractal topology-analysis [Grassberger, 1983] and applied to higher dimensional attractors obtained by delay-coordinate-embedding [Packard et al., 1980; Takens, 1981]. Although revealing astonishing significances in separating suspicious data from surrogate-based null hypothesis [Schreiber and Schmitz, 1997], they can only be obtained by huge computational effort and lack the ability to clearly separate linear from nonlinear features. Fractal- or correlation-dimension estimates are further often unable to distinguish static from dynamic properties.

To identify non-Gaussianities in the Cosmic Microwave Background, it turned out very beneficial to search for correlations or anomalies in the phases of spherical harmonics[8]. Very recently, a similar approach has been used to uncover nonlinearities induced by surrogate generation algorithms [Räth et al., 2012] by seeking correlations in the Fourier phases. Moreover, fundamental scaling properties of highly nonlinear financial time series have exactly been reproduced by imposing a set of linear corre-

[1] [Richman and Moorman, 2000; Hoyer et al., 1997; Andrzejak et al., 2001]

[2] [Pascual et al., 2000; Altizer et al., 2006]

[3] [Vautard and Ghil, 1989; Kurths and Herzel, 1987; Vio et al., 1992]

[4] [Alvarez-Ramirez et al., 2002; LeBaron, 1994; Strozzi et al., 2002]

[5] [Ivanov et al., 1999; Lehnertz and Elger, 1998; Ho et al., 1997]

[6] [Golestani and Gras, 2014]

[7] [Birkholz et al., 2015]

[8] See for example [Coles and Chiang, 2000; Coles et al., 2004; Stannard and Coles, 2005; Chiang and Coles, 2000; Chiang et al., 2002, 2003, 2007; Wu, 2007a,b; Sung et al., 2010; Modest et al., 2014]

lations on the Fourier phases of Gaussian white noise [Räth and Laut, 2015].
In fact, from the definition of the linear time series traits alone it already follows by the Wiener-Khinchin-Theorem that all nonlinear properties are constrained to the Fourier phases[9]. Yet, to the best of the author's knowledge, no measure exists so far to extract phase information.

The substance of this thesis is an attempt to show *how* Fourier phases take effect on nonlinear time series features (and vice versa) and to employ this concept to derive a novel class of nonlinearity tests. It starts with a short introduction into commonly used tools (Chapter 2) and continues with an analytic study of the relationship between certain nonlinear events and the Fourier phases (Chapter 3). The main focus here is on leptokurtic data, that is, data showing heavy-tailed probability distribution functions. Next, in Chapter 4 some methods and techniques are developed that help to extract the features expected to appear and a few analysis results for experimental and simulated data are presented in Chapter 5. Finally, a short conclusion at the end briefly summarizes the contents and results and gives an outlook on possible further implementations and strategies.

[9] A detailed explanation is presented in Section 2.3.

Chapter 2

Nonlinearities in Time Series

2.1 Linear and Static Time Series Features

Many time series show statistical features that can be divided into two categories. First, there are properties that stretch over the whole time series (global properties), neglecting temporal correlations. These properties are fully represented by the probability distribution function (PDF) of the time steps in real space and can be further abstracted as the *statistical moments*. This category will also be referred to as *static*. It may contribute to the linear as well as to the nonlinear regime. The second is the temporal or *dynamic* properties of the time series. These features may as well stretch globally over the whole data or be variable in time. Since the differentiation of these two kinds is one of the major subjects treated in this work, a more detailed view on the distinctive characteristics of the both is presented in the following.

2.1.1 Static Time Series Properties

As mentioned above, all static properties are given by the PDF of the investigated time series in real space. Since practical applications do usually not demand to know the exact shape of the PDF it is often sufficient to describe it by a few values that can be derived from the statistical moments

$$\mu_{n,c} = \langle (x-c)^n \rangle_x = \int_{-\infty}^{\infty} (x-c)^n p(x) dx. \tag{2.1}$$

In the discrete case they can also be written as

$$\mu_{n,c} = \langle (x-c)^n \rangle_x = \sum_x (x-c)^n p(x). \tag{2.2}$$

Here, $\mu_{n,c}$ is the n^{th} statistical moment about the value c of the PDF $p(x)$. The notation $\langle \circ \rangle_x$ is used for the expectation value of a variable $\circ$ averaged over x in

Meaning	Derivation	Related moments
Mean μ	$\mu := \mu_{1,0} = \langle x \rangle_x$	1
Variance σ^2	$\sigma^2 := \mu_2 = \langle (x-\mu)^2 \rangle_x$	1, 2
Skewness γ_1	$\gamma_1 := \frac{\mu_3}{\sigma^3} = \frac{\langle (x-\mu)^3 \rangle_x}{\sigma^3}$	1, 2, 3
Kurtosis γ_2	$\gamma_2 := \frac{\mu_4}{\sigma^4} - 3 = \frac{\langle (x-\mu)^4 \rangle_x}{\sigma^4} - 3$	1, 2, 4

Table 2.1: Important statistical values and their relation to the first four statistical moments.

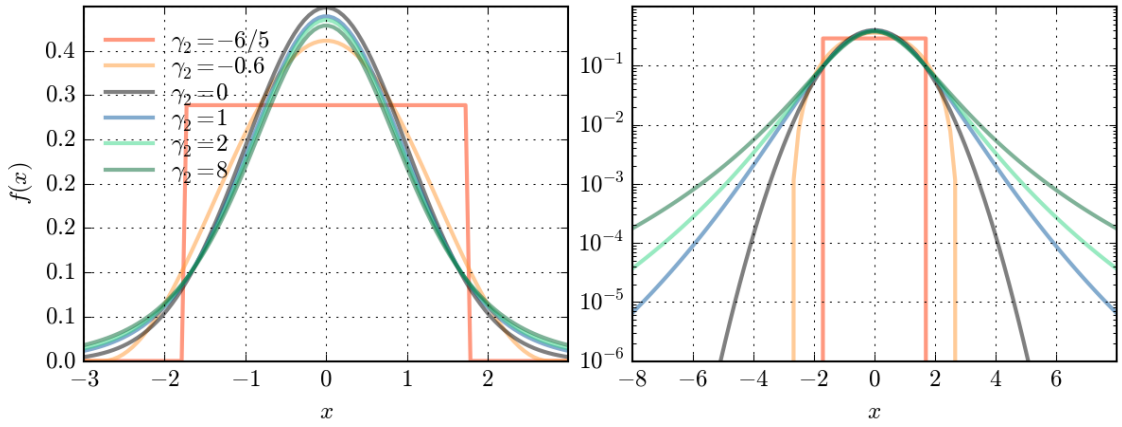

Figure 2.1: Various centered probability density functions with normalized standard deviation: Platykurtic uniform distribution with $\gamma_2 = -6/5$, platykurtic raised cosine distribution ($f(x) = 1/2s[1 + \cos(\pi x/s)]$ with $s = \sigma/\sqrt{1/3 - 2/\pi^2}$) with $\gamma_2 = -0.6$, mesokurtic normal distribution with $\gamma_2 = 0$ and three leptokurtic Student's t-distributions ($\gamma_2 = 1$, $\gamma_2 = 2$, $\gamma_2 = 8$). The distributions with $\gamma_2 > 0$ decay much slower towards distant values than the normal distribution. The resulting *tails* are often referred to as *fat tails* or *heavy tails*.

both, either in the discrete or in the continuous case. $\mu_n := \mu_{n,\mu_{1,0}}$ with only one index refers to the n^{th} *centered* moment. The first four moments are used to distill some prominent and important descriptors in statistical data analysis. A brief overview is given in Tab. 2.1. The square root of the variance, σ, is also called the *standard deviation* and describes the variation of values around the mean. The skewness γ_1 measures the asymmetry of a distribution. Finally the *excess kurtosis* [Kenney and Keeping, 1951] - or simply kurtosis - γ_2 describes the behavior of the distribution's "tails". If γ_2 is negative, the distribution is said to be *platykurtic* and *leptokurtic* if it is positive. The latter case is of great importance in this work. Leptokurtic distributions are also called *fat-tailed* or *heavy-tailed*. If γ_2 is equal to 0, the distribution is *mesokurtic*, which is the case for Gaussian distributions. See Fig. 2.1 for some typical representations of the various cases.

2.1.2 Dynamic Time Series Properties

The most commonly computed dynamic time series properties are the *linear* ones, which are defined as all that are captured in an autoregressive (AR) model [Whitle, 1951; Box and Jenkins, 1976] of the general form

$$\tilde{x}_t = \mu + \sum_{i=1}^{p} c_i \tilde{x}_{t-i} + \epsilon_t. \tag{2.3}$$

Here, c_i are the model parameters, ϵ_t is Gaussian white noise with variance σ_ϵ^2 and p is the order of the AR process (AR(p)). $\tilde{\mathbf{x}} = \{\tilde{x}_t\}_{t=0}^{N-1}$ is a time series, generated by the AR process, with N time steps. This definition constrains the quantifiable dynamic linear properties to μ and the c_i. The latter are chosen such that the process optimally reproduces the behavior of the investigated time series $\mathbf{x}$. The probably most convenient way to obtain these parameters is by means of the autocorrelation function (ACF)

$$\mathcal{A}(\tau) = \frac{\langle (x_t - \mu)(x_{t+\tau} - \mu) \rangle_t}{\sigma^2} \tag{2.4}$$

where σ is the standard deviation of $\mathbf{x}$ and the numerator $\langle (x_t - \mu)(x_{t+\tau} - \mu) \rangle_t =: cov(x_t, x_{t+\tau}) = \mathcal{C}(\tau)$ is the *autocovariance*. $cov(\circ, \diamond)$ denotes the *covariance* between $\circ$ and $\diamond$. The c_i can be constructed by the Yule-Walker equations [Yule, 1927; Walker, 1931]:

$$\mathcal{C}(\tau) = \sum_{i=1}^{p} \mathcal{C}(\tau - i) \cdot c_i + \sigma_\epsilon^2 \delta_{\tau,0}. \tag{2.5}$$

$\delta_{\tau,0}$ is the Kronecker delta[1]. Multiplying all equations with $\tau \neq 0$ by σ_2 yields

$$\mathcal{A}(\tau) = \sum_{i=1}^{p} \mathcal{A}(\tau - i) \cdot c_i \tag{2.6}$$

or equally

$$\begin{bmatrix} \mathcal{A}(1) \\ \mathcal{A}(2) \\ \vdots \\ \mathcal{A}(p) \end{bmatrix} = \begin{bmatrix} \mathcal{A}(1-1) & \mathcal{A}(1-2) & \cdots & \mathcal{A}(1-p) \\ \mathcal{A}(2-1) & \mathcal{A}(2-2) & \cdots & \mathcal{A}(2-p) \\ \vdots & \vdots & \ddots & \vdots \\ \mathcal{A}(p-1) & \mathcal{A}(p-2) & \cdots & \mathcal{A}(p-p) \end{bmatrix} \begin{bmatrix} c_1 \\ c_2 \\ \vdots \\ c_p \end{bmatrix}. \tag{2.7}$$

The one remaining equation for $\tau = 0$ can be solved as well, once the $\{c_i\}_{i=1}^p$ are determined by Eq. 2.6. Note that $\mathcal{A}(-\tau) = \mathcal{A}(\tau)$. In this form it is clear that Eq. 2.6 is a bijection between the autocorrelation coefficients $\mathcal{A}(\tau)$ and the AR coefficients c_i. Hence, it follows that ***all* linear properties can as well be expressed by the ACF coefficients**. To gain some intuition about how time series can behave if purely generated by a linear process, consider the following two cases, or combinations of both.

[1] $\delta_{i,j} = 1$ if $i = j$ and 0 else.

Harmonic oscillations
An AR process can describe a periodic harmonic oscillation or a superposition of such oscillations.

Exponential decay and growth
An AR model can lead to an exponential decay or growth.

All other phenomena that may occur in a linear process are stochastic variations, induced by an external noise source ϵ_t.

2.2 Nonlinear Time Series Analysis

Nonlinear time series properties, as the term itself obviously implies, are all properties that are not linear. Hence, by definition it is all features not represented by the autocorrelation coefficients. To imagine those, consider *every* time series behavior that is neither a harmonic oscillation nor an exponential decay nor a Gaussian random fluctuation. The variety is infinite. In the following, an attempt is made to categorize some different types of nonlinear behavior just to gain a little more overview.

2.2.1 Static Nonlinearities

The perhaps simplest type of nonlinearity is the *static* type, where a linear stochastic process dependent on time $L(t)$ serves as the input of a nonlinear function $f(x)$. The outcome is a process $S(t) = f(L(t))$, that shows nonlinearities in its PDF but not in any temporal aspect. If $f(t)$ is bijective and $S(t)$ has a stable mean μ_S and a finite, stable variance σ_S, $L(t)$ can near-completely be reconstructed by mapping $S(t)$ onto a Gaussian PDF with mean μ_M and variance ${\sigma_M^2}^2$. The choice of μ_M defines the offset of the reconstructed time series $L'(t)$, and σ_M^2 its standard deviation. In any case, if $L(t)$ is a linear process, also $L'(t)$ is one. Thus, nonlinearities of *solely* static kind can be isolated and in some cases even be identified.

2.2.2 Dynamic Nonlinearities

Maybe the simplest example of a dynamic nonlinear process $D(t)$ would be a linear process $L(t)$ that is multiplied by a function of time $g(t)$, which is no linear process by itself: $D(t) = L(t) \cdot g(t)$. Note that the multiplication alone is a linear operation and only the nonlinear variability of one factor over time induces the nonlinearity. This type could for example occur in remote sensing devices, where the measured signal travels through a dynamically changing medium (e.g. air) before it reaches the sensor. If the modulating distortion $g(t)$ is much slower than the observed process,

[2] A linear process has a Gaussian PDF by default (see Appendix A.3 and Sec. 4.2). Hence, except for the initial mean μ_L and variance σ_L^2, $L(t)$ can be completely reconstructed.

one way of getting rid of it, is to distill the envelope function $e(t)$ and normalize the measured signal by it: $L' = D(t)/e(t)$. Also, if some knowledge about the modulating medium or the signal source exists, simple dynamic nonlinearities can be detected and isolated. In general though, it is substantially impossible to reconstruct $g(t)$ from the recorded data.

Furthermore, most types of dynamic nonlinearities in stochastic time series can of course not be modeled by a simple multiplication with a modulation function. Often dynamic nonlinearities are not even visible at first sight.
To overcome theses difficulties, a lot of measures and tools to classify and quantify nonlinearities have been developed in the past. Some of them will be presented in the next section.

2.2.3 Common Measures and their Limitations

In this section, a few common measures and tools are introduced that are routinely used in nonlinear time series analysis. Although not all of these are relevant to the analysis later conducted in this work, they are mentioned anyway to present a brief overview over the state-of-the-art methods in the field. For simplicity and shorter notation, the measures are defined for *centered* signals, i.e.

$$x_t = x_t - \langle x_t \rangle \tag{2.8}$$

which of course implies that the signal x_t has a finite mean $\langle x_t \rangle$.

2.2.3.1 Higher Order Correlation Functions

The probably most obvious extension of the set of linear analysis tools that were encountered in Section 2.1 are the higher order autocovariance functions:

$$\mathcal{C}^n(\tau) = \langle x_t \cdot x_{t-\tau} \cdot x_{t-2\tau} \cdots x_{t-n\tau} \rangle_t. \tag{2.9}$$

Here, not only two points in time are correlated but n.

2.2.3.2 Time Reversibility

Another quantity, somehow similar in form to higher-order covariance functions, is the time-reversibility [Schreiber and Schmitz, 1997]:

$$\mathcal{T}(\tau) = \left\langle (x_{t+\tau} - x_t)^3 \right\rangle_t = 3 \left[\left\langle x_{t+\tau} x_t^2 \right\rangle_t - \left\langle x_{t+\tau}^2 x_t \right\rangle_t \right]. \tag{2.10}$$

Significant deviations of $(T(\tau))$ from 0 indicate that the signal is not invariant under time reversal. Although this "is a sufficient and powerful indicator of nonlinearity", it is "not a necessary condition", as already Schreiber and Schmitz mentioned. In the next sections some measures and techniques are introduced that may be a little more sophisticated in their derivation but do very successfully manage to overcome this problem.

2.2.3.3 Embedding

Packard et al. [1980] suggested a method to reconstruct a multidimensional phase space picture from a one dimensional time series by using *delay coordinates*:

$$\mathbf{x}_i = \{x_i, x_{i+\tau}, x_{i+2\tau}, \ldots, x_{(d-1)\tau}\} \tag{2.11}$$

For experimental time series, the delay time τ is suggested to either be determined by the first zero-transition or the first minimum of the ACF or of the mutual information [Shannon, 1948; Cover and Thomas, 1991]. The embedding dimension d can for example be estimated using the method of false nearest neighbors [Kennel et al., 1992]. The idea is, that the time steps of the embedded time series may be too close together, only because they are projected into a space of too low dimension. Thus, one starts with a low embedding dimension and successively increases it until a proper ratio between false and true nearest neighbors is reached. Takens [1981] proved that the reconstructed multi-dimensional time series – also called *attractor* – is topologically equivalent to the one the experimental time series originated from. Hence, this embedding technique enables many measures from chaos- and complex systems-theory to be applied to experimentally obtained data sets.

2.2.3.4 Lyapunov Exponent

The Lyapunov exponent [Lyapunov, 1892, 1992; Bylov et al., 1966] characterizes the divergence of infinitesimally close trajectories in time. For a known iteration $x_{t+1} = f(x_t)$, the Lyapunov exponent is given by

$$\lambda = \lim_{t\to\infty} \frac{1}{N} \sum_{t=0}^{N-1} \ln(f'(x_t)) \tag{2.12}$$

where $\circ'$ denotes the derivative of $\circ$ with respect to x_t in this case. If the exponent is greater than 0, the flow diverges and if it is smaller than 0, it converges. For an experimental time series, $f(x_t)$ is most likely unknown and λ can thus not be computed this way. One method to estimate it though was suggested by Kantz [1994]:

$$S(\tau) = \left\langle \ln \left[\frac{1}{|\mathcal{U}_t|} \sum_{x_i \in \mathcal{U}_t} |\mathbf{x}_{t+\tau} - \mathbf{x}_{i+\tau}| \right] \right\rangle_t \tag{2.13}$$

$$\lambda = \frac{\delta S(\tau)}{\delta \tau} \tag{2.14}$$

Here, $\mathcal{U}_t$ is a spherical volume with radius ϵ around a data point x_t. x_i are data points that are located within this sphere, i.e., they can be regarded as origins of neighboring trajectories. If the distances of the data points that follow x_i to those that follow x_t remain the same in average, the attractor behaves predictable and the Lyapunov exponent, which is basically the slope of the logarithm of the normalized distances, stays small. The Lyapunov exponent is therefore a measure of how chaotic or unpredictable a system behaves.

Approach	Method
Fixed Ball	$f_\tau(\mathbf{x}_t) = \frac{1}{\lvert\mathcal{U}_\epsilon\rvert} \sum_{\mathcal{U}_\epsilon} \mathbf{x}_{i+\tau}$
Soft Ball	$f_\tau(\mathbf{x}_t) = \frac{1}{\lvert\mathcal{U}_\epsilon\rvert} \sum_{\mathcal{U}_\epsilon} w_i \mathbf{x}_{i+\tau}$
Fixed Mass	$f_\tau(\mathbf{x}_t) = \frac{1}{N_{nn}} \sum_{i=0}^{N_{nn}-1} \mathbf{x}_{i+\tau}$

Table 2.2: Three different options to get the average over the trajectory movement in the neighborhood of a data point $\mathbf{x}_t$. $f_\tau(\mathbf{x}_t)$ is the predicted coordinate $\mathbf{x}_{t+\tau}$ after τ time steps, $\mathcal{U}_\epsilon$ is the spherical region around $\mathbf{x}_t$ and w_i is a weighting factor (e.g. $w_i = e^{-\lvert\mathbf{x}_t - \mathbf{x}_i\rvert^2/\sigma_\epsilon^2}$).

2.2.3.5 Nonlinear Prediction Error

A similar approach to characterizing chaotic behavior in time series is the nonlinear prediction error (NLPE) [Farmer and Sidorowich, 1987; Sugihara and May, 1990]. The idea is to predict the trajectory of a chosen data point by averaging over the trajectories of its neighboring data points. If the prediction diverges significantly from the real path, chaotic dynamics are assumed to underlie the process.
To perform this analysis, one starts again with embedding the time series into a more dimensional phase space. Then, one data point $\mathbf{x}_t$ is selected and a set of corresponding neighbors is determined by either selecting all points in a spherical region around $\mathbf{x}_t$ (*fixed ball* or *soft ball*) or by taking a fixed number of nearest neighbors N_{nn} (*fixed mass*). In the first approach one can choose between a simple or a weighted sum over all points within the sphere. See Tab. 2.2 for a more detailed description.
The next step is to calculate the temporal mean of the squared distances between prediction and real trajectory over all times t. The NLPE finally becomes the square root of this mean:

$$\Psi(\tau) = \left\langle [f_\tau(\mathbf{x}_t) - \mathbf{x}_{t+\tau}]^2 \right\rangle_t^{\frac{1}{2}} \tag{2.15}$$

2.2.3.6 Generalized Dimensions

The last kind of measures to be addressed here are the generalized dimensions. The formulation that is most convenient for use in time series analysis was probably given by Grassberger [1983]. Since a detailed derivation would go beyond the frame of this chapter, the generalized dimension is introduced just by its definition:

$$\mathcal{D}_q = \lim_{\epsilon \to 0} \frac{I_q(\epsilon)}{\ln(\frac{1}{\epsilon})} = \frac{1}{q-1} \lim_{\epsilon \to 0} \frac{d \ln(C_q(\epsilon))}{d \ln(\epsilon)} \tag{2.16}$$

with the order-q correlation integral

$$C_q(\epsilon) = \left\langle \langle \Theta(\epsilon - r_{ij}) \rangle_{i \neq j}^{q-1} \right\rangle_j = \frac{1}{N} \sum_{j=0}^{N-1} \left[\frac{1}{N-1} \sum_{i=0, i \neq j}^{N-1} \Theta(\epsilon - r_{ij}) \right]^{q-1}. \tag{2.17}$$

Here, r_{ij} is the Euclidean distance between the embedded data points $\mathbf{x}_i$ and $\mathbf{x}_j$, $\Theta(\circ)$ is the Heaviside step function[3], ϵ is a distance threshold, and q is the index of the dimension. I_q is the Rényi information [Rényi, 1961]. The derivative in Eq. 2.16 is to be understood as the slope of a (linear) fitting function for very small values of ϵ in a numerical analysis.
Generalized dimensions are usually employed in analysis where the actual value of the questioned time series is compared to a null distribution derived from surrogates (see Sec. 4.8). The result alone can in general not hint to nonlinear features without external reference.
In the following analysis however generalized dimensions will not be utilized as reference measures, since they deliver no better results than the NLPE for time series analysis (see [Schreiber and Schmitz, 1997]).

There exist much more measures or varieties than those presented so far, but these are presumable the most reliable and common ones in nonlinear time series analysis. A few of them will therefore accompany us through the remainder of this work and serve as references for later analysis.
In the next section, a concept is introduced that enables a very clear confinement of nonlinear traits and the derivation of a new class of measures.

2.3 Wiener-Khinchin-Theorem

Let us first provide an adequate convention for the continuous Fourier transform:

$$F(k) = \int_{-\infty}^{\infty} f(t) e^{i2\pi kt} dt. \tag{2.18}$$

Its inverse is then given by

$$f(t) = \int_{-\infty}^{\infty} F(k) e^{-i2\pi kt} dk. \tag{2.19}$$

This form is generally more relevant to the theoretical treatment of problems than to the practical, since experimental data is usually obtained in discretized form. In this case one can use the following transformation to switch to Fourier space

$$F(k) = \sum_{t=0}^{N-1} f(t) e^{i2\pi kt/N}. \tag{2.20}$$

[3] $\Theta(\circ) = 1$ if $\circ > 0$ and $\Theta(\circ) = 0$ if $\circ < 0$. An analytic expression is for example given by $\Theta(\circ) = d/dx(\max\{0; \circ\})$. For the current case, it is convenient to further define that $\Theta(0) = 1$, so that all distances including ϵ are counted.

The corresponding inverse transform is then given by

$$f(t) = \frac{1}{N} \sum_{k=0}^{N-1} F(k) e^{-i2\pi kt/N}. \tag{2.21}$$

An extremely useful and famous quantity that can directly be derived from the Fourier transform is the *power spectrum* or the *spectral density*:

$$\mathcal{P}(k) = x^*(k) \cdot x(k) = |x(k)|^2. \tag{2.22}$$

$\circ^*$ denotes the complex conjugate of $\circ$. $\mathcal{P}(k)$ *"describes how the variance of the data x(t) is distributed over the frequency domain"*[4].
The power spectrum of a stationary random process is directly linked to the autocorrelation function by a Fourier transform:

$$\mathcal{P}(k) = \frac{1}{2\pi} \int_{-\infty}^{\infty} \mathcal{A}(\tau) e^{i2\pi k\tau} d\tau. \tag{2.23}$$

This relation is known as the Wiener-Khinchin-Theorem [Wiener, 1930]. A proof is given in Appendix A.1. The Fourier transform, as a complex function or series, can generally also be written as $F(k) = |F(k)|e^{i\phi(k)}$, where $|\circ|$ indicates the modulus of $\circ$ and $\phi(k)$ are the Fourier phases.

Historically it may have had its first practical application in 1955 for an analog correlator system for brain potentials [Barlow and Brown, 1955]. Until the mid twentieth century Fourier transforms were carried out by mechanical Fourier analyzers [Otnes, 2008] which provided good results for smooth and regular data but unfortunately not for noisy, stochastic time series [Wiener, 1961]. Barlow and Brown recorded electroencephalograms on magnetic tapes and played them back by a special device with two magnetic pick-up heads separated by a variable distance τ. The two output signals were then multiplied by an analog circuit and fed into an integrator (low pass filter) consisting of a resistor and a capacitor. At a fixed distance τ (that of course corresponds to a time difference), the tapes were completely played back and the integrator averaged over the product of the two signals $s(t)$ and $s(t+\tau)$. The voltage at the integrator is hence directly proportional to the ACF $\mathcal{A}(\tau)$ of the recordings.
In the next steps, the tapes were reversed and played back again for further values of τ and the voltage was measured each time, until the whole ACF was constructed successively. Due to the averaging, the result became a relatively smooth function, that could then easily serve as the input for a mechanical harmonic analyzer which finally revealed the power spectrum.

Nowadays the Wiener-Khinchin-Theorem still finds a practical application in computing the ACF from the power spectrum (ironically the exact opposite direction

[4]Phrasing borrowed from [Wikipedia, 2015].

as in 1955), which, in turn, can easily be calculated by very efficient and often even hardware-accelerated Fourier transform algorithms. This can lead to much shorter computation times compared to deriving the ACF directly by repeatedly averaging over the time series product for various τ.

For the current purpose, the Wiener-Khinchin-Theorem will help to enclose all nonlinear time series properties into a finite set of numbers.

From Eq. 2.6 it already became clear that all linear time series properties are represented by the ACF. On the other hand, the Wiener-Khinchin-Theorem (Eq. 2.23) provides a bijective mapping between the ACF and the power spectrum. Hence, all linear information must be fully represented by the power spectrum as well. Since the power spectrum is just the squared absolute values of the Fourier transform (see Eq. 2.22), all remaining necessary information to reconstruct the time series $f(t)$ is the Fourier phases $\phi(k)$.

It follows that *all nonlinear information resides in the Fourier phases*. In the following chapters, this concept will be employed to find a novel time series analysis tool that is exclusively sensible to nonlinearities.

Chapter 3

Analytic Description

In this chapter, an unusual description of a leptokurtic time series is used to derive its effect on the phases in Fourier space analytically. Although the following time series are discrete in general, the temporal dependence is indicated with brackets $\circ(t)$ instead of indices $\circ_t$ to avoid confusion with other indices.

3.1 Leptokurtosis as Superimposed δ-Peaks

To construct a simple leptokurtic time series $\xi(t)$, consider first a series of uncorrelated Gaussian random variables $\eta(t)$ with finite standard deviation σ_η and vanishing mean $\mu_\eta = 0$. The power spectrum of this series does of course not show significant irregularities and is statistically flat over the whole range of frequencies (white noise). Also the Fourier phases of $\eta(t)$ do not show any anomalies[1].
To induce heavy tails, some of the data points now get shifted away from the mean:

$$\xi(t) = \eta(t) + \sum_{j=0}^{P-1} a_j \delta(t - \tau_j). \tag{3.1}$$

Here a_j is the additive magnitude (the amount of shift) of the j^{th} data point (*outlier*) at the temporal position τ_j. P is the total number of outliers and $\delta(t - \tau_j) = 1$ if $t = \tau_j$ and 0 else. Thus, $\xi(t)$ can simply be written as a superposition of Gaussian noise and some delta functions. $\xi(t)$ is certainly a very rude approximation for usually appearing experimental leptokurtic time series, but it is perfectly suited for an analytic treatment and suffices to explain basic effects of heavy tails. Fig. 3.1 illustrates an example for $P = 3$ and $\sigma_\eta = 1$. The kurtosis reaches a high value of $\gamma_2 = 111.9$.
Let us now turn our attention to the Fourier representation.

[1]Further details in Section 4.2

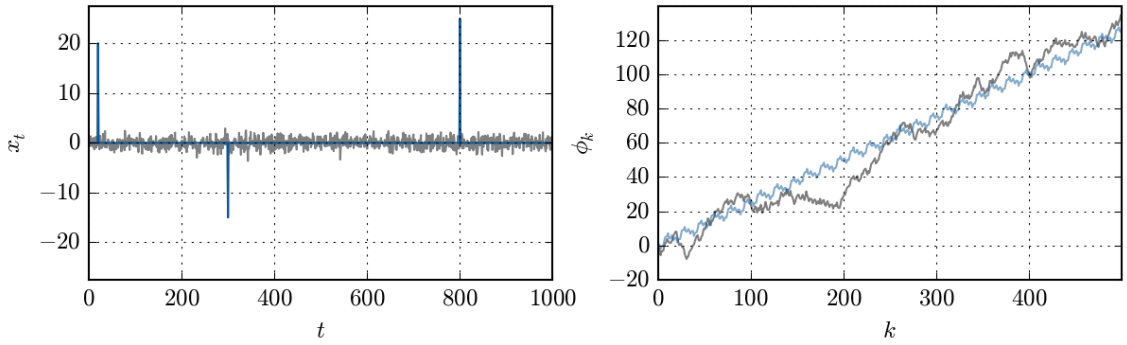

Figure 3.1: Left: Some data points (in this case $P = 3$) of white Gaussian noise (gray) are shifted (blue) to construct outliers similar to those in time series with heavy tails. The blue curve corresponds to $\xi(t) - \eta(t)$ (see Eq. 3.1). Right: The Fourier phases of $\xi(t) - \eta(t)$ (blue) and $\xi(t)$ (gray). Both show a common overall trend and some oscillations although only three samples share similar values.

3.2 Effects on the Fourier Phases

A discrete Fourier transform according to Eq. 2.20 of $\xi(t)$ yields

$$\Xi(k) = H(k) + \sum_{j=0}^{P-1} a_j e^{i2\pi \frac{\tau_j}{N} k} = H(k) + \sum_{j=0}^{P-1} A_j(k). \tag{3.2}$$

$H(k)$ is the discrete Fourier transform of $\eta(t)$. It becomes clear that also the Fourier representation of $\xi(t)$ is a superposition of $H(k)$ and some complex numbers $A_j(k)$ that represent vectors of length a_j and angle

$$\phi_j(k) = \frac{2\pi\tau_j}{N} k \propto k \tag{3.3}$$

in the complex plane. For all $\tau_j \neq 0$, the angle increases with k and for $\tau_j = 0$, also ϕ_j becomes zero.
To illustrate the effect of the $A_j(k)$, consider the simplest case of only one dominating outlier represented in Fourier space by $A_0(k)$. The phase $\Phi(k)$ of $\Xi(k)$ then becomes the angle of the sum of the two vectors $A_0(k)$ and $H(k)$. To obtain an outlier with a significant leptokurtic effect, $|A_0(k)| = a_0$ is required to strongly dominate over $|H(k)|$. Hence, $\Phi(k)$ will be $\phi_j(k)$ plus a relatively small random fluctuation around 0, since the direction, or phase of $H(k)$ is randomly and uniformly distributed for Gaussian noise. As $\phi_j(k) \propto k$, also $\Phi(k)$ grows linearly with k.
If there is more than one outlier, a more complicated but still vivid picture in the complex plane might be imagined. The noise floor $H(k)$ can still be regarded as random numbers with a relatively small magnitude compared to the a_j and a uniformly distributed direction. The $A_j(k)$ however, rotate with a slope of

$$\dot{\phi}_j = \frac{d\phi_j}{dk} = \frac{2\pi\tau_j}{N} \tag{3.4}$$

as k increases. Note, that also the slope increases as the temporal position τ_j of the spike moves from the beginning of the time series to its end. In the complex plane, this corresponds to a chain of rotating vectors with a small random fluctuation, given by $H(k)$. If the number of outliers with roughly equal magnitude is large (this would not meet the assumption of leptokurtosis), this results in a chaotic mixture of cycles and epicycles. But if there is still a limited number of dominating outliers, an overall trend in the rotation of $\Xi(k)$ can be recognized. (This is of course the case for leptokurtic and especially scale-free PDFs.) The right-hand graph in Fig. 3.1 shows the phases for this type of situation with three distinctive outliers. Another point to mention is that the direction of the vector $\Xi(k)$ can also be essentially steered into one particular direction, if the $A_j(k)$ rotate nearly coherently with k. This happens, if many τ_j share roughly equal values, corresponding to a cumulation of outliers and hence, to a burst event in the time series.
The artificial construction of leptokurtic noise according to Eq. 3.1 leads to a useful description of the behavior in Fourier space.
In the next chapter, some tools are introduced and developed to extract features like those from the Fourier phases of experimental time series.

Chapter 4

Methodology

4.1 Unwrapping

A number in the complex plane can be considered as a vector with a certain length – the modulus – and a certain angle – the phase. The latter are cyclic with a period of 2π. I.e. a number with a phase of α is equal to a number with the same modulus and a phase of $\alpha \mod 2\pi$. Therefore, the phases of the Fourier coefficients can be constrained to an interval of length 2π, which can freely be chosen to start at $-\pi$:

$$I_\phi = \{x \in \mathbb{R} | -\pi < x \leq \pi\} \tag{4.1}$$

As a consequence, possible trends or long-range correlations in a series of phases may become hard to detect. Linear trends for example might result in sawtooth behavior (see Fig. 4.1 (left)). To overcome this problem in a limited scope, a technique known as *phase tracking* or *unwrapping* can be utilized. For the methods covered in this work, it suffices to use the presumably simplest and most famous algorithm, introduced by Itoh in 1982.

The differences between two consecutive, wrapped[1] phases can simply be written as

$$\Delta\phi(k) = \phi(k+1) - \phi(k). \tag{4.2}$$

To construct the differences of the *unwrapped phases* $\Delta\phi'(k)$, the following recursion rule can then be applied:

$$\Delta\phi'(k) = \begin{cases} \Delta\phi(k) - 2\pi & \text{if } \Delta\phi(k) > +\pi \\ \Delta\phi(k) + 2\pi & \text{if } \Delta\phi(k) \leq -\pi \\ \Delta\phi(k) & \text{else} \end{cases} \tag{4.3}$$

Intuitively speaking, every clockwise phase difference gets reinterpreted as counter-clockwise if it exceeds $+\pi$ and vice versa if it falls below $-\pi$. The unwrapped phases

[1] The phases that are constrained to I_ϕ are called "wrapped". A numerical Fourier transform self-evidently returns wrapped phases by default.

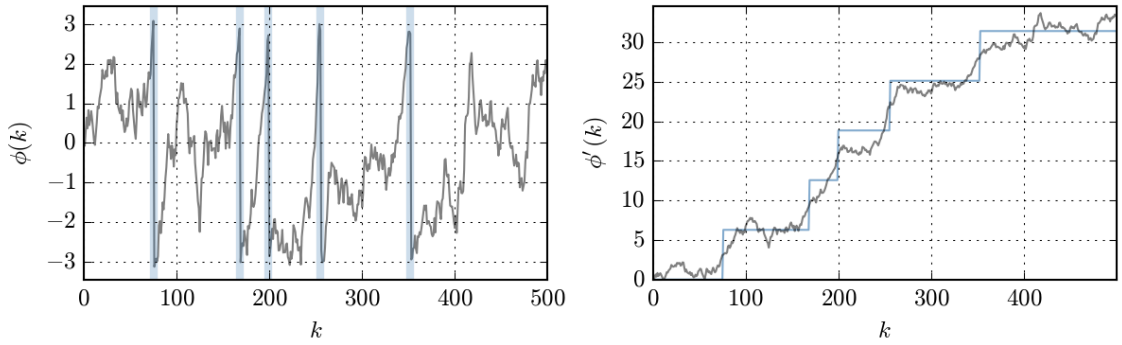

Figure 4.1: Left: A linear trend in the Fourier phases results in a sawtooth behavior, when the phases get *wrapped* into the interval I_ϕ. The blue vertical lines indicate wraps. Right: The unwrapped phases (gray) and the accumulated changes caused by the unwrapping procedure (blue).

are then obtained by a cumulative sum over the differences with $\phi'(0) = \phi(0) = 0$[2].

$$\phi'(k) = \sum_{i=0}^{k-1} \Delta\phi'(i) \tag{4.4}$$

Noisy data, which is by far the most common case in time series analysis, can induce so called *fake wraps* [Itoh, 1982; Jenkinson, 2003]. This motivated the development of more sophisticated unwrapping algorithms (see for example Ghiglia and Pritt [1998]). Most of them though assume the Nyquist criterion [Nyquist, 1928] and a relatively high signal-to-noise ratio, which is not in general the case for experimental data. Especially the Nyquist criterion is not fulfilled by the data that is later considered for analysis. Moreover, Eq. 3.4 implies that $\dot{\phi}_j$, which is equivalent to $\Delta\phi(k)$ in the model case, exceeds π if τ_j lies in the second half of the time series, leading to fake wraps intrinsically. Therefore, fake wraps can indeed not be excluded completely, but extensively sufficient for the current purpose.
Note here that, due to the periodicity of the phases, the unwrapping procedure leaves the Fourier phases in a modified state which, however, has no consequence for the Fourier representation at all. A back transformation of a Fourier representation of a time series with wrapped phases would yield the very same time series as of one with unwrapped phases.

Important to mention is that Eq. 4.4 happens to show a form that can be recognized as a one-dimensional random walk [Pearson, 1905], if it is rewritten as

$$\phi'(k+1) = \phi'(k) + \Delta\phi'(k). \tag{4.5}$$

[2]The 0^{th} phase belongs to the Fourier mode that describes the offset. As this mode has a frequency of 0 and is hence just a constant, it is invariant under phase shifting. $\phi(0)$ can therefore freely be chosen to be 0.

More precisely, Eq. 4.5 describes a discretized Wiener process [Wiener, 1923] without drift. This inspires us to refer to the unwrapped phases as *phase walks*. In the following section some statistical properties of the unwrapped phases as well as of their differences are derived for uncorrelated, Gaussian noise.

4.2 Statistical Properties of Phase Walks

Let us start with a stochastic time series of independent and identically distributed Gaussian random variables – Gaussian white noise. "White" means that it shows a statistically constant power spectrum and hence, no linear temporal correlation (see A.2). In fact, Gaussian white noise is also obtained by maximizing the entropy of an arbitrary time series with finite mean and variance (a proof is given in Appendix A.3). In Fourier space, a maximization of entropy with a given power spectrum (that is Fourier amplitudes), results in random, independent and identically distributed Fourier phases (a proof is provided in Appendix A.4):

$$P_{\phi(k)}(x) = \begin{cases} \frac{1}{2\pi} & \text{if } -\pi < x \leq \pi \\ 0 & \text{else} \end{cases} . \tag{4.6}$$

$P_\circ(\diamond)$ denotes the PDF of a random variable $\circ$ at the value $\diamond$.
The distribution of the phase differences then becomes

$$\begin{aligned} P_{\Delta\phi(k)}(x) = P_{\phi(k+1)-\phi(k)}(x) = \int_{-\infty}^{+\infty} P_{\phi(k)}(y) \cdot P_{\phi(k+1)-x}(y) \cdot dy = \\ \frac{1}{4\pi^2} \int_{-\pi}^{+\pi} \left\{ \begin{array}{ll} 1 & \text{if } -\pi < y+x \leq \pi \\ 0 & \text{else} \end{array} \right\} \cdot dy = \begin{cases} \frac{1}{2\pi} + \frac{x}{4\pi^2} & \text{if } -2\pi < x < 0 \\ \frac{1}{2\pi} - \frac{x}{4\pi^2} & \text{if } 0 \leq x \leq 2\pi \\ 0 & \text{else} \end{cases} . \end{aligned} \tag{4.7}$$

This is a triangular shaped PDF, symmetric around 0 and spanning from -2π to 2π. To obtain the distribution function of the steps of the unwrapped phases, one can straightforwardly *wrap*[3] Eq. 4.7:

$$P_{\Delta\phi'(k)}(x) = \begin{cases} P_{\Delta\phi(k)}(x) + P_{\Delta\phi(k)}(x+2\pi) & \text{if } -\pi < x < 0 \\ P_{\Delta\phi(k)}(x) + P_{\Delta\phi(k)}(x-2\pi) & \text{if } 0 \leq x \leq \pi \\ 0 & \text{else} \end{cases} . \tag{4.8}$$

Hence, the steps of the unwrapped phases are distributed uniformly between $-\pi$ and π just like the steps between the wrapped phases:

$$P_{\Delta\phi'(k)}(x) = P_{\phi(k)}(x) = \begin{cases} \frac{1}{2\pi} & \text{if } -\pi < x \leq \pi \\ 0 & \text{else} \end{cases} \tag{4.9}$$

[3]Wrapping is the inverse of unwrapping: $\phi^{wrapped} = [(\phi + \pi) \mod 2\pi] - \pi$

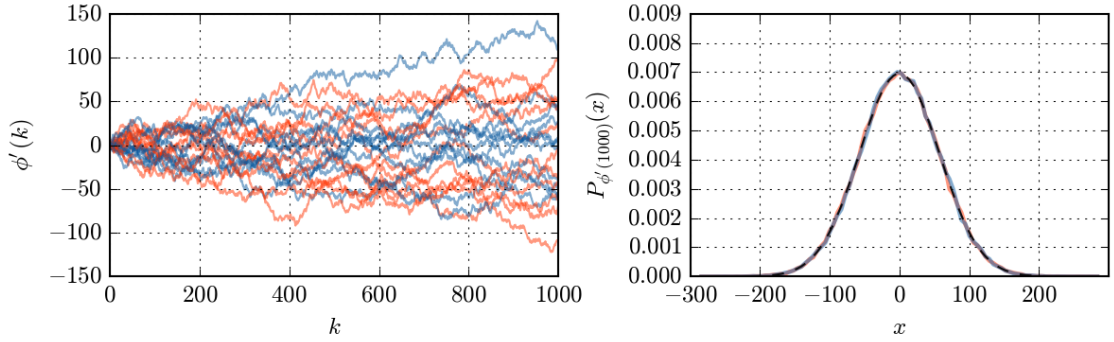

Figure 4.2: Left: Nine realizations of artificially generated random walks with uniform step distribution according to Eq. 4.9 (red) and phase walks, obtained by unwrapping the phases of Gaussian white noise (blue). Right: Empirical distribution functions of the random walks (red) and the phase walks (blue) after $k = 1000$ steps. The dashed line corresponds to a Gaussian normal distribution with variance $\frac{\pi^2}{3} \cdot 1000$.

Thus, the series $\phi'(k)$ does indeed behave like a true random walk with an independent uniform step distribution in the case of Gaussian white noise. We can therefore continue with finding an expression for the variance of the phase walk itself.

From the central limit theorem [Pólya, 1920; Feller, 1945] it follows that the distribution of a random walk with independent and identically distributed steps will converge to a normal distribution after a sufficient number of steps. The corresponding variance is given by the variance of the step distribution σ_1^2 times the step index i [Wiener, 1923]:

$$\sigma_i^2 = i \cdot \sigma_1^2 \tag{4.10}$$

The proof can be found in Appendix A.5. The variance of $P_{\Delta\phi'(k)}(x)$, which corresponds to the step distribution, is

$$\sigma_1^2 = \int_{-\infty}^{\infty} x^2 P_{\Delta\phi'(k)}(x)\, dx = \int_{-\pi}^{\pi} x^2 \frac{1}{2\pi}\, dx = \frac{\pi^2}{3} \tag{4.11}$$

and hence, the variance of the phase walk after k steps becomes

$$\sigma_k^2 = \frac{\pi^2}{3} k. \tag{4.12}$$

Fig. 4.2 visualizes this result by illustrating the empirical distribution functions of ideal random walks, phase walks of Gaussian white noise and a normal distribution with the theoretically derived variance for reference. Comparing the variance of empirical phase walks to the variance from Eq. 4.12 lends itself as a good criterion to decide whether a phase walk is really random or biased in any sense. This can be achieved by means of an adjusted version of a classical *variance ratio test*. If the phases behave truly independent and random according to Eq. 4.12, they are said to fulfill the *random walk hypothesis*.

$\mathcal{S}(\kappa)$	Interpretation
$\ll 1$	Phase walk is likely to be centered around zero.
$0-3$	Phase walk is likely to fulfill the random walk hypothesis.
$\gtrsim 3$	Phase walk is likely to have a trend.

Table 4.1: Interpretation of SRT results.

4.3 Variance Ratio Test

Lo and MacKinlay [1988] introduced a test to show that stock prices do not behave like ideal random walks. They argued that for the latter, the variance of the increments should directly scale with the distance over which is incremented. This is equivalent to Eq. 4.10. Even if σ_1^2 is unknown, the following condition should be satisfied

$$\frac{\sigma_{a\cdot\tau}^2}{a\cdot\sigma_\tau^2} \approx 1. \tag{4.13}$$

Lo and MacKinlay basically used violations of this equation to show that stock market time series do not behave like ideal random walks.
In the current work, deviations from ideal random walk behavior in the unwrapped Fourier phases are detected by comparing variances computed from experimentally gathered data with the theoretical variances from Eq. 4.12. The former are calculated by averaging (similar to the method presented by Cochrane [1988]). The experimental variance is then given by

$$\sigma_\kappa^2 = \left\langle [\phi'(k+\kappa)-\phi'(k)]^2 \right\rangle_k = \frac{1}{K-\kappa}\sum_{k=0}^{K-\kappa-1}[\phi'(k+\kappa)-\phi'(k)]^2 \tag{4.14}$$

where K is the number of phases and κ is the phase index difference. From that, one can now define a quantity that measures the deviation from the random walk hypothesis as

$$\mathcal{S}^2(\kappa) = \frac{3\cdot\left\langle [\phi'(k+\kappa)-\phi'(k)]^2 \right\rangle_k}{\pi^2} = \frac{3\sum_{k=0}^{K-\kappa-1}[\phi'(k+\kappa)-\phi'(k)]^2}{\pi^2\kappa[K-\kappa]}. \tag{4.15}$$

4.4 Standard Deviation Ratio Test (SRT)

To obtain a more intuitive ratio of standard deviations rather than a ratio of variances, also $\mathcal{S}(\kappa)$ can be used by simply taking the square root of Eq. 4.15. This test is also referred to as the *standard deviation ratio test* (SRT) from now on.
Tab. 4.1 provides interpretations of various co-domains of $\mathcal{S}(\kappa)$. As it turned out in Section 3.2, leptokurtic time series tend to induce trends, that is non-zero slopes, into the Fourier phases. As an example, Fig. 4.3 (left) shows SRT results of the artificial

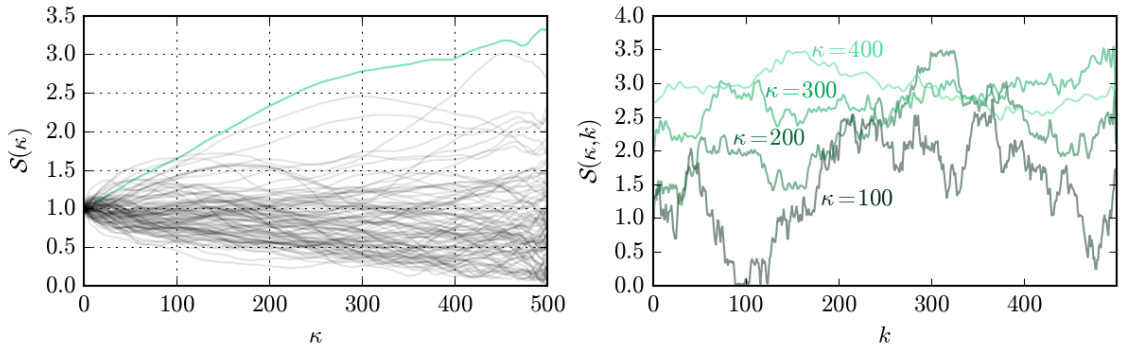

Figure 4.3: Left: Standard deviation ratio test (SRT) for 100 time series of Gaussian white noise (gray) and for the time series with three shifted data points (green) from Eq. 3.1/Fig. 3.1. The modified time series shows a relatively steep increase in $\mathcal{S}(\kappa)$, while the results for Gaussian noise basically stay below 3. Right: The frequency dependent SRT at four fixed values of κ. (The curves are stretched to the proper length.)

time series $\xi(t)$ from Eq. 3.1, that is also pictured in Fig. 3.1, and of Gaussian white noise. In Section 5.1, the connection between leptokurtosis and Fourier phase correlations is studied and quantified in further detail.

4.4.1 Frequency Dependent SRT

Another way to characterize a phase walk is to not average over the increments to get σ_κ^2 (see Eq. 4.15), but to simply compare the moduli of the increments $|\phi'(k+\kappa) - \phi'(k)|$ at various index positions k to the reference standard deviations $\sqrt{\kappa \cdot \sigma_1^2}$:

$$\mathcal{S}(\kappa, k) = \sqrt{\frac{3}{\pi^2 \kappa}} \cdot |\phi'(k+\kappa) - \phi'(k)| \tag{4.16}$$

Although the increments alone are not valid estimators for the corresponding standard deviations of course, this analysis (*frequency dependent SRT*) can reveal which frequency bands have the strongest impact on phase correlations. Fig. 4.3 (right) shows $\mathcal{S}(\kappa, k)$ of the artificial time seres from Fig. 3.1 for four different values of κ. The mean of each curve (not explicitly shown) is just $\mathcal{S}(\kappa)$ for the corresponding κ (left figure). For none of those curves a striking deviation from being constant over all ks can be observed. This agrees with Section 5.1, where we obtained that shifts of single time steps affect all Fourier phases.
On the other hand, a slow nonlinear process (without any high frequency components) that is distorted by uncorrelated Gaussian white noise should for example carry no nonlinear information in its high frequency modes. The phases in this region should therefore fulfill the random walk hypothesis, while for low indices they should not. Fig. 4.4 illustrates the results for a time series that has been generated to fit this criteria. The slow nonlinear components of the pictured time series have been crafted by iteratively adjusting the PDF of a low-pass filtered Gaussian random process to

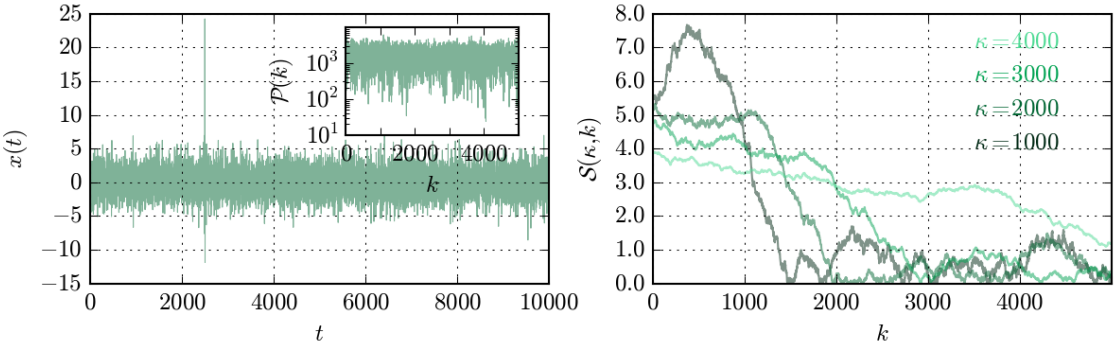

Figure 4.4: Left: Artificially generated time series that is a superposition of a slow nonlinear process and Gaussian white noise. The small embedded window shows the corresponding power spectrum. Right: Frequency dependent SRT for the time series. All curves exhibit very high values for low frequencies and clearly decrease with higher frequencies k, indicating that the underlying nonlinear process dominates at low frequencies. Non frequency dependent $\mathcal{S}(\kappa)$ reaches a maximum of 3.54 at $\kappa = 4985$ (not visible in the figure).

become leptokurtic (the procedure is also outlined in Section 4.8.3). Subsequently, uncorrelated Gaussian white noise has been added to generate unbiased high frequency modes. $\mathcal{S}(\kappa, k)$ appropriately detects the nonlinearities on the low frequency scales while not displaying any significance for the higher modes.

4.5 SR-Maps

Another way to illustrate $\mathcal{S}(\kappa, k)$ is to color-code the values on a two-dimensional k-κ-map (SR-map). Fig. 4.5 shows the SR-map for the time series from Eq. 3.1/Fig. 3.1 (in sub-figure B) and for its background noise $\eta(t)$ (in sub-figure A). (Hence, the upper two images correspond to Fig. 4.3.) Here, $\mathcal{S}(\kappa, k)$ increases quite continuously with κ and shows no significant trends in k-direction.
Further, the SR-map for the artificial time series from Fig. 4.4 is pictured in sub-figure D and for its background noise in sub-figure C. (Hence, the lower two images correspond to Fig. 4.4.) Here, it is now clearly visible that $\mathcal{S}(\kappa, k)$ increases massively at low frequencies, while for high frequencies only regular variations appear until κ spans over both frequency bands. Note that the pattern, produced by the background noise, in the areas where nonlinear influence does not occur is exactly the same for both images. Also notice that in the region around $\kappa \approx 500$ and $k \approx 800$ the test result reaches up to ≈ 8.
SR-maps might be useful to identify specific time scales that are subject to nonlinear influence. For the toy example from Fig. 4.4 they even revealed that nonlinearities were only present in the low frequency bands. Other nonlinearity measures known to the author are not able to accomplish this without evaluating and comparing several band-pass-filtered versions of the time series. This would of course only be a

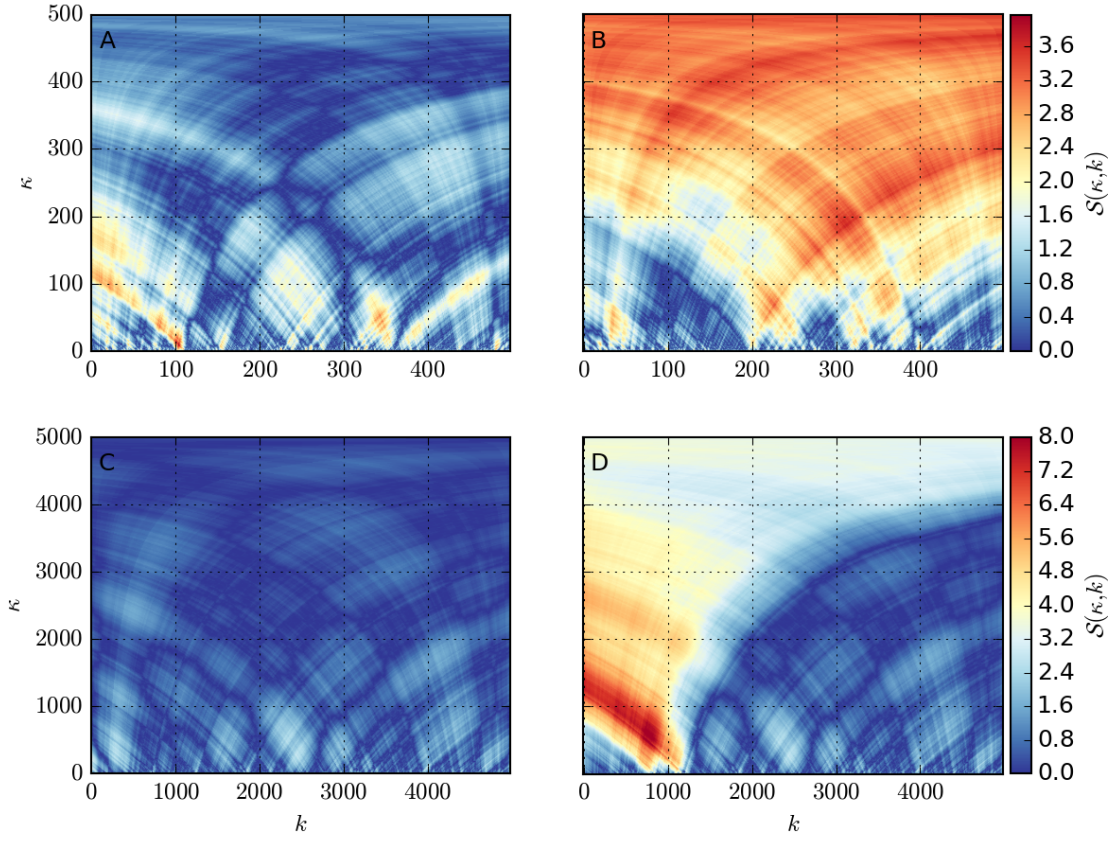

Figure 4.5: SR-maps for various time series: A: Background noise $\eta(t)$ of Eq. 3.1/Fig. 3.1. B: $\xi(t)$ from Eq. 3.1/Fig. 3.1. C: Background noise of the time series in Fig. 4.4. D: Time series from Fig. 4.4.

workaround and no intrinsic feature of the measure.

In the next section, some tricks and methods are introduced to manipulate or prepare time series to enhance the significance of the SRT.

4.6 Rotating SRT

From Eq. 3.4 it became clear that the slope of a phase walk may depend on the positions of prominent outliers. Further, it has already been noticed in Section 4.1 that the unwrapping procedure is not able to properly recognize slopes that are greater or equal to π. If they are greater, the slopes are interpreted as being negative and if they are equal, the unwrapped phase steps statistically fluctuate between π and $-\pi$, effectively adding up to zero. It therefore suggests itself to *rotate* the time series. Applying the rotation operator to a time series $\{x(t)\}_{t=0}^{T}$ with T time steps by an amount τ can be written as

$$\mathcal{R}^{\tau}(\{x_t\}_{t=0}^{T}) = \{\{x_t\}_{t=T-\tau}^{T}; \{x_t\}_{t=0}^{T-\tau}\}. \tag{4.17}$$

For example

$$\mathcal{R}^{3}(\{0;1;2;3;4;5;6;7;8;9\}) = \{7;8;9;0;1;2;3;4;5;6\}. \tag{4.18}$$

Sometimes it may also be convenient to express the amount of rotation by an angle $\rho = 360° \cdot \tau/T$.
The rotation does not change the linear time series properties, since those are equivalent to the moduli of the Fourier coefficients. Applying a Fourier transform automatically implies the assumption of a periodic function. The relative position of this signal (also called the *phase* of the signal) to a reference index is encoded in the Fourier phases alone and hence, a rotation does not affect the power spectrum. In some cases it is therefore advisable to mask the time series with a window function [Harris, 1978] prior to the Fourier analysis to reduce artifacts from discontinuities between the first and the last time step.
For time series with roughly continuous transitions between the last and the first time step and maybe even high frequency components, it is however not unalterably a requirement to use them. Imagining the time series spliced to a closed ring, this becomes intuitively clear: A harsh discontinuity at the splice of a smooth time series naturally falsifies both the linear and the nonlinear features, as it corresponds to an event that is very untypical for the rest of the time series[4]. Yet, a splice in a centered and noisy time series might not even be visible to the unaided eye. For the both examples we already exhaustively used in the previous sections, it is for example definitely valid to do so. Fig. 4.6 shows a sequence of twelve rotated versions of the time series $\xi(t)$ from Eq. 3.1/Fig. 3.1. While $\xi(t)$ caused a maximum SRT result of ~ 3.3, $\mathcal{R}^{150°}(\xi(t))$ elevates it to ~ 5.8. Another way of illustrating the SRT results

[4]See Section 5.6 for an example.

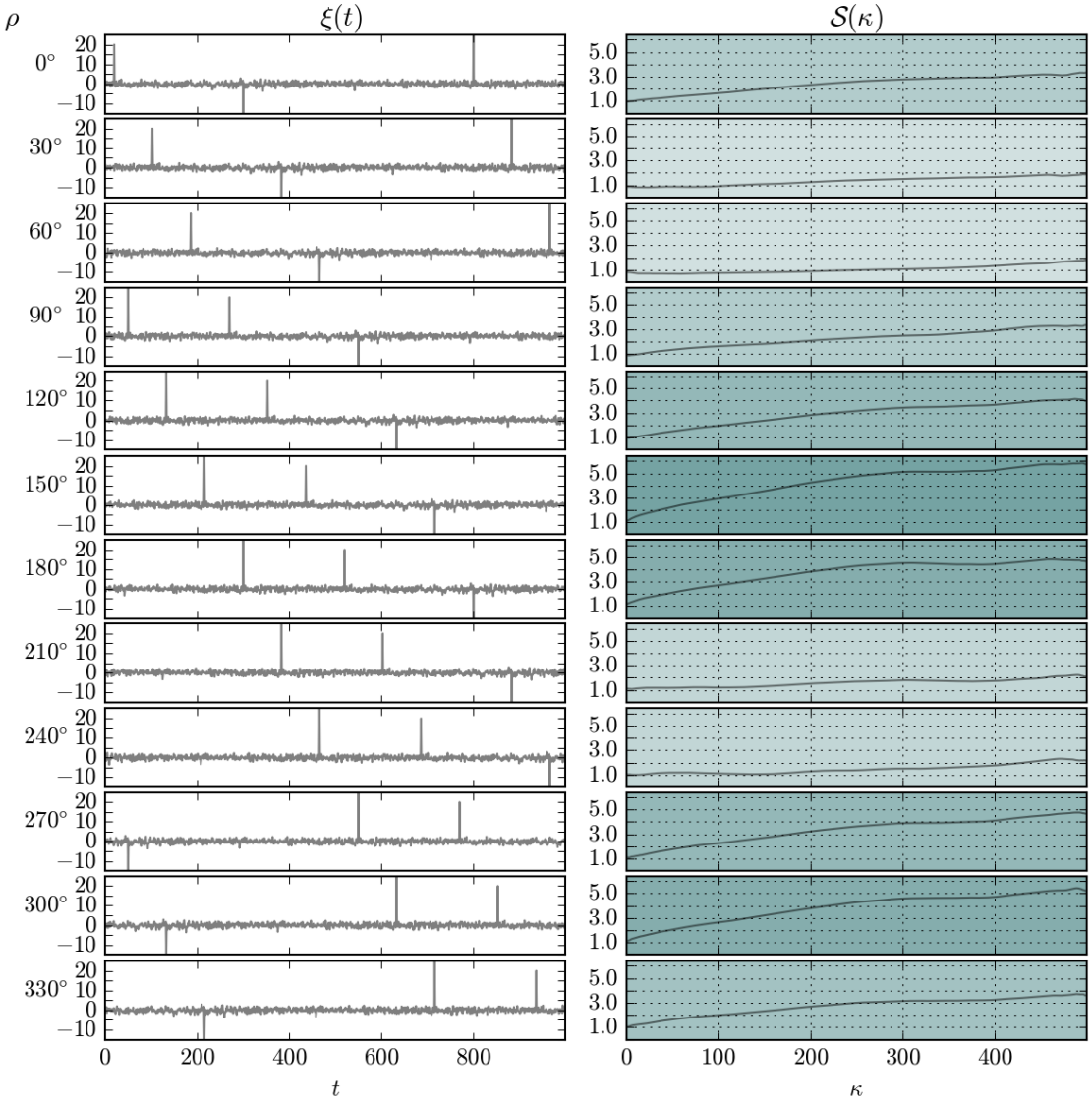

Figure 4.6: Left column: Versions of $\xi(t)$ (Eq. 3.1/Fig. 3.1) for different rotation angles ρ. Right column: SRT results for each of the versions. The saturation of the background is proportional to the maximal value of $\mathcal{S}(\kappa)$.

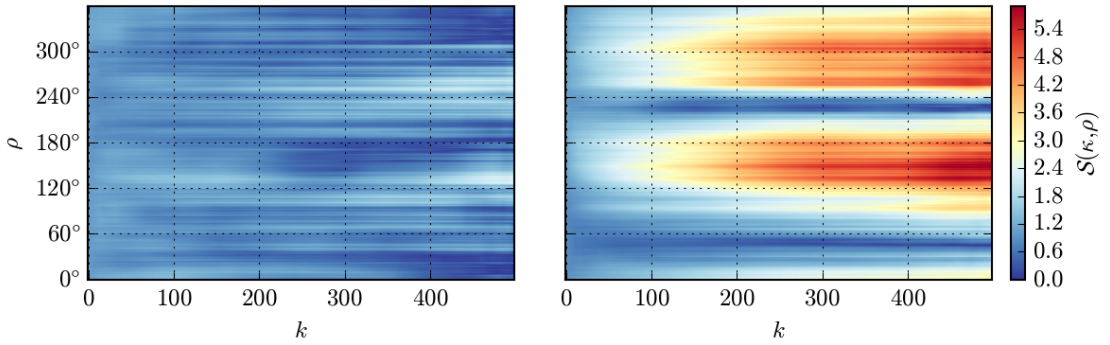

Figure 4.7: Left: $\mathcal{S}(\kappa)$ of the background noise $\eta(t)$ (Eq. 3.1/Fig. 3.1) for different rotation angles ρ. Right: Same for the modified time series $\xi(t)$.

for different rotation angles is again to color-code it on a two-dimensional k-ρ-map. Fig. 4.7 illustrates this for $\xi(t)$ (right) and its background noise $\eta(t)$ (left). Since rotating alone does not induce any further nonlinearities relevant in Fourier space as those that were already present in the time series, it might be justified to use it for time series preparation prior to analysis. One should though bear in mind that this does not necessarily hold true for other nonlinear measures.

4.7 Inpainting

As stated in the previous section, window functions are sometimes used to reduce distortions of the Fourier spectrum by edge effects. Although this is a well established and verified method, it severely falsifies the PDF. While this might be negligible in many cases, it disadvantageously impacts the analysis presented in the current work. For the time series where we encounter significant discontinuities between the last and the first sample it therefore seems reasonable to seek alternatives.

As explained before, it is clever for any Fourier application to picture the time series as a closed ring that is spliced between the last and the first time step. The idea is to smooth out a possible discontinuity at the splice by inserting a patch between the two ends that attaches continuously and basically matches the linear properties of the time series. Methods to produce such patches have been proposed and very successfully been applied for image reconstruction [Bertalmio et al., 2000; Elad et al., 2005; Pires et al., 2009]. They are referred to as *inpainting* techniques. The present analysis will orient itself towards an algorithm proposed by Elad et al. [2005]. Here it is assumed that there exists a dictionary Φ, such that the original signal X can be completely represented by a *sparse* set of coefficients α_i as $\Phi\alpha = X$. The dictionary Φ could for example consist of wavelets [Mallat, 1989], ridgelets [Candès and Donoho, 1999] or curvelets [Starck et al., 2003], i.e. a transform that is *overcomplete*. Here, overcomplete is to be understood as that more than one set α can exactly reproduce X in real space.

The first problem is now to find one such representation that is sparse, i.e. the number of non-zero coefficients α_i shall be small. This set would somehow represent the minimal information needed to fully describe the data with the *words* accessible in Φ. The idea is to mask the part of the data that is to be reconstructed and let an algorithm find the sparsest description, while reproducing the unmasked regions. The masked areas should therefore attain features as closely related to the unmasked data as possible. This can be achieved by minimizing

$$||\alpha||_0 = \sum_i (1 - \delta_{\alpha_i,0}) \tag{4.19}$$

such that

$$||Y - MX||^2 \leq \sigma. \tag{4.20}$$

Here, $\delta_{\alpha_i,0}$ is 1, if α_i is 0 and 0 else. $||\circ||_0$ is the l_0-pseudo-norm, which is just the number of non-zero elements and $||\circ||$ is the Euclidean length $\sqrt{\sum_i \circ_i^2}$. M is the mask ($M_i = 0$ if masked and 1 else) and $Y = \Phi\alpha$ is the reconstructed data. The algorithm Elad et al. proposed, called MCA, solves this problem by iteratively adjusting Y as

$$Y_{n+1} = \Delta_{\Phi,\lambda_n}[Y_n + M(X - Y_n)]. \tag{4.21}$$

$\Delta_{\Phi,\lambda_n}[\circ]$ represents an operator that first performs a transformation $\Phi^T\circ$, second thresholds the resulting components α_i such that only components $\alpha_i \geq \lambda_n$ survive and third transforms them back by $\Phi\alpha$. λ_n is decreased after each step.

Sato et al. [2010] utilized inpainting for the first time to fill gaps in time series instead of pictures. They succeeded in restoring the power spectra of heavily distorted data to a quite satisfactory extend by choosing a mixture of a discrete cosine transform and a wavelet transform as their dictionary Φ.

In the studies conducted for the present work however, it turned out that a standard Fourier transform suffices to inpaint gaps in time series. It may even be better suited for the current purpose since – in contrast to image reconstruction, where nonlinear interpolation certainly leads to more convincing results – superposing of Fourier modes alone is substantially a linear operation. The algorithm used for the later analysis can therefore be outlined as follows:

1. Set all unmasked data points of the inpainted time series y equal to those of x: $y \leftarrow y + M(x - y)$.

2. Compute the Fourier transform:
   $\tilde{y} \leftarrow \mathrm{FT}(y)$

3. Threshold the Fourier modes:
   $\tilde{y}^k \leftarrow \begin{cases} \tilde{y}^k & \text{if } \tilde{y}^k > \epsilon \\ 0 + 0i & \text{else} \end{cases}$

4. Back transform to real space:
   $y \leftarrow \mathrm{IFT}(\tilde{y})$.

5. Decrease ϵ and repeat steps 1 - 5 until ϵ is sufficiently small.

The quality of the result very sensitively depends on the function with which ϵ decreases. In the present work, it turned out most favorable for many time series to choose this function proportional to $1/i^2$, where i is the iteration index. Yet, the decrease function should carefully be adjusted to the particular data set. If, for example, two principal regimes of Fourier mode amplitudes are present, it might even be considered to use two different transitions for each regime.

Examples for successful applications of the inpainting technique can be found in sections 5.6, 5.7 and 5.8.

4.8 Surrogates

In Section 4.4, a null hypothesis that represents Gaussian white noise has already been defined (Eq. 4.12). In the analysis of real data however, it is often interesting to compare the test results to null hypotheses that reflect some more sophisticated properties. In this section four methods to generate surrogate data sets are introduced that reproduce the linear properties and / or the PDF of a model time series. The measure of choice can then be applied to each of the generated *surrogates* such that a distribution of test results appears: the *null distribution*.

4.8.1 FT Surrogates

A very easy and computationally efficient surrogate algorithm consists of randomizing the Fourier phases of the original data [Theiler et al., 1992]. These so called FT (Fourier-transformed) surrogates are basically linear Gaussian processes sharing all linear properties of the original time series. All other properties, including the PDF of course, are lost. The steps can easily be summarized as

1. Fourier-transform the data.

2. Randomize the phase of each Fourier coefficient.

3. Back-transform the data.

4.8.2 AAFT Surrogates

Amplitude adjusted Fourier-transformed surrogates [Theiler et al., 1992] are intended to reproduce both the linear features and the PDF of the model time series. The algorithmic steps are

1. *Rank-ordered remap* the data to a Gaussian PDF[5].
2. Execute the three steps of the FT algorithm.
3. Rank-ordered remap the data back to its original PDF.

The so obtained surrogates exactly reproduce the original PDF but only approximately reproduce the linear properties, since the last step obviously influences them again (remapping whitens the power spectrum). Schreiber and Schmitz [1996] showed that AAFT surrogates can lead to a false indication of nonlinearities in linear time series.

4.8.3 IAAFT Surrogates

To overcome this problem Schreiber and Schmitz [2000] introduced the *iterated amplitude adjusted Fourier-transformed* (IAAFT) surrogates. The algorithm can be structured into the following steps.

1. Store the PDF and the power spectrum of the original time series and shuffle the time steps.
2. Fourier-transform the data and adjust the power spectrum to match the stored version.
3. Back-transform the data and rank-ordered remap it to the stored PDF.
4. Repeat step 2. and 3. consecutively for a defined number of times or until no further change occurs. In any case the procedure stops after adjusting the power spectrum (and back-transforming of course).

4.8.4 Simulated Annealing

The last surrogates introduced here are the SA (simulated annealing) surrogates [Schreiber, 1998]. The corresponding algorithm is somewhat different from those stated so far:

1. Compute and store the autocorrelation function $\mathcal{A}_{target}(\tau)$ of the time series and shuffle all time steps.
2. Calculate and cache the autocorrelation function $\mathcal{A}_{pre}(\tau)$, then swap two randomly chosen samples.
3. Compute the autocorrelation function $\mathcal{A}_{act}(\tau)$ and the differences $d_{pre} = ||\mathcal{A}_{target}(\tau) - \mathcal{A}_{pre}(\tau)||$ and $d_{act} = ||\mathcal{A}_{target}(\tau) - \mathcal{A}_{act}(\tau)||$. If $d_{act} \leq d_{pre}$, keep the two samples swapped. Else, reverse the swapping with a probability $exp(-(d_{act} - d_{pre})/T)$.

[5]This means that a series of Gaussian random numbers as well as the data are sorted by the value of its samples, while the index of the time series samples is remembered. Then each data sample is substituted with the corresponding random number and finally it is resorted by the index.

4. Reduce T by a small amount and repeat steps 2. - 4. until d_{pre} is sufficiently small.

The parameter T controls the acceptance of a swap that caused the autocorrelation function to move into the "wrong" direction. It is therefore analogous to a process that slowly looses temperature. Simulated annealing produces very good results but is computationally extremely time-intense. Hence, it can practically not be used to generate huge numbers of surrogates.

One further point to mention is that shuffling a time series causes its power spectrum to whiten, since all temporal correlations are destroyed. Hence, surrogates for time series with inherent white power spectra can simply be generated by shuffling the original data. The linear properties are then reproduced statistically, which may be even more favorable than reproducing them exactly [Dolan and Spano, 2001].
In the following analysis particularly the just described shuffling and the IAAFT surrogates are employed to construct the null distributions.

Chapter 5

Results

5.1 Nonlinear Effects of Leptokurtic PDFs

The first result presented in this section is the distribution of SRT results for leptokurtic random time series. A parametrized Pearson-type IV distribution [Pearson, 1916], namely Student's t-distribution [Student, 1908; Fisher et al., 1925] determines the PDF of independent and identically distributed random samples with predefined kurtosis γ_2:

$$P_{\gamma_2}(x) = \frac{\Gamma\left(\frac{5}{2}+\frac{3}{\gamma_2}\right)}{\sqrt{2\pi\left(1+\frac{3}{\gamma_2}\right)}\Gamma\left(2+\frac{3}{\gamma_2}\right)}\left(1+\frac{x^2}{2+\frac{6}{\gamma_2}}\right)^{-\frac{5}{2}-\frac{3}{\gamma_2}} \tag{5.1}$$

For eight different values of γ_2, 10^5 noise series with $2 \cdot 10^4$ samples where created to obtain empirical PDFs of the corresponding SRT results. To capture long range phase correlations, $\mathcal{S}(\kappa)$ is evaluated at a high phase index difference $\kappa = 9800$. (The total number of phases is $K = 10000$.) Additionally to the leptokurtic, one set of platykurtic noise time series and one of mesokurtic was generated. The former is a uniform distribution with

$$P_U(x) = \begin{cases} \frac{1}{\sqrt{12}} & \text{if } x \in \left[-\sqrt{12}/2, \sqrt{12}/2\right] \\ 0 & \text{else} \end{cases}. \tag{5.2}$$

The standard deviation of this distribution is equal to that of Student's t-distribution (Eq. 5.1) $\sigma_{p_U} = \sigma_{p_{\gamma_2}} = 1$ and the mean is also $\mu_{p_U} = 0$ of course. The kurtosis of a uniform distribution on the other hand is negative $\gamma_2 = -6/5$.
For the mesokurtic noise, a Gaussian distribution with consistent mean $\mu_{p_G} = 0$ and standard deviation $\sigma_{p_G} = 1$ perfectly suites its purpose.

Let us first analyze the statistical effect of leptokurtosis on the SRT. As clearly visible in Fig. 5.1, the distribution of $\mathcal{S}(\kappa)$ broadens dramatically as γ_2 increases. In other words, high values of $\mathcal{S}(\kappa)$ and hence phase walks with non-zero slopes are more and

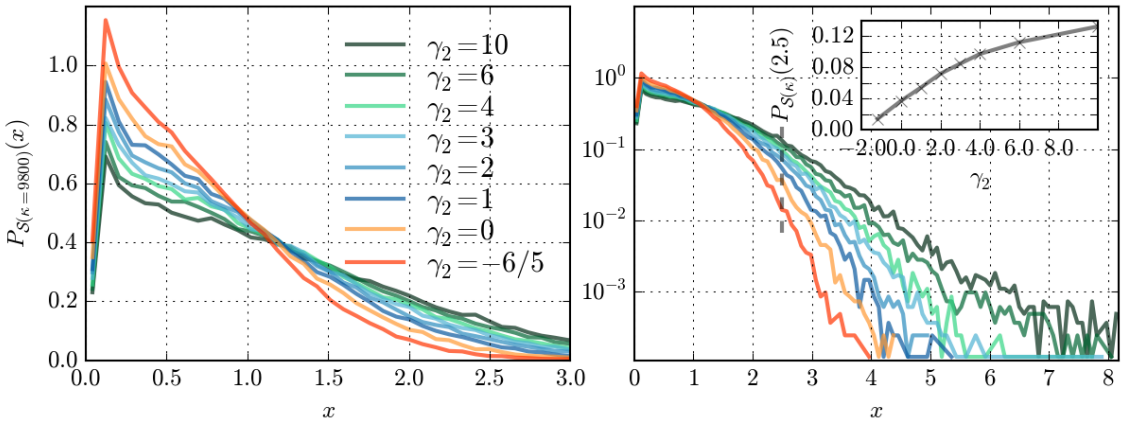

Figure 5.1: Left: PDFs of the SRT results for noise with varied kurtosis on a linear scale. Right: Same PDFs on a logarithmic scale. The small embedded window shows a slice (indicated by the dashed gray line) through the PDFs at $x = 2.5$. The probability density increases monotonically with γ_2.

more likely to appear as the kurtosis increases, which is in excellent agreement with the analytic results from Chapter 3.2.
The distribution for Gaussian noise ($\gamma_2 = 0$) is equivalent to the distribution of representatives of the random walk hypothesis (see Sec. 4.2). Also note that in this case, the probabilities do indeed roughly match those given by the number of standard deviations $\mathcal{S}(\kappa)$[1].
Maybe the most unexpected outcome however is that platykurtic noise causes the $\mathcal{S}(\kappa)$-PDF to narrow. This means that phase walks of platykurtic time series are centered by tendency. On the one hand, it is clear that platykurtic PDFs have nonlinear origin and therefore non-random phases. On the other hand, it seems not obvious how platykurtosis induces centering of phase walks. Since this work is especially dedicated to leptokurtic time series however, let us take this as a remarkable observation and turn our attention back to the heavy-tailed time series.

The first result demonstrated that phase walk analysis can be used to statistically precisely quantify the static nonlinear effect of non-Gaussian PDFs. The following sections will focus on dynamic features of empirical time series.

[1]Statistical significance is often given in multiples of the standard deviations of a normal distribution.

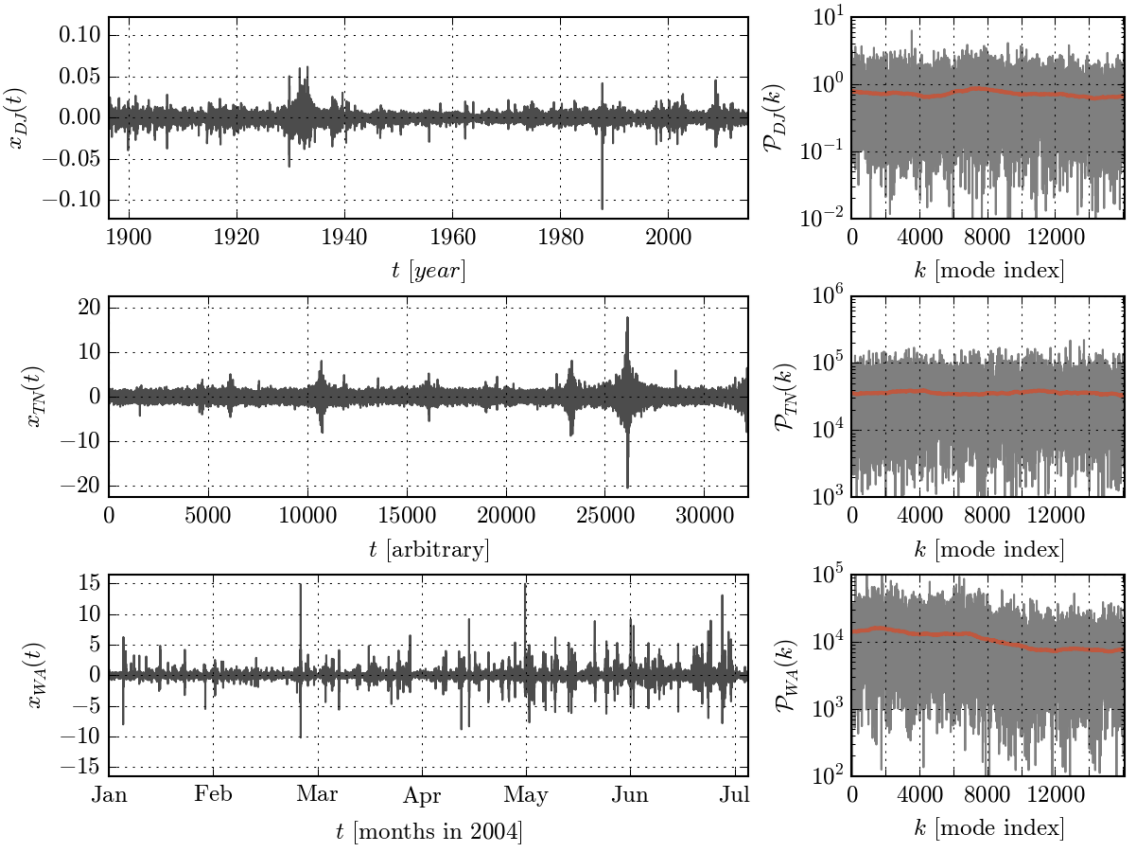

Figure 5.2: Top: Logarithmic daily returns of the Dow Jones Industrial Average from 26$^{\text{th}}$ of May 1896 until 23$^{\text{rd}}$ of October 2014. Mid: Artificial time series with tailored nonlinearities. Bottom: Wind acceleration measured at an Atlantic offshore wind turbine from January, 1$^{\text{st}}$, 2004, 00:10 until Juli, 10$^{\text{th}}$, 2004, 18:20 with a sampling period of 10 minutes.
On the right of each time series is the corresponding power spectrum (gray) and its trend (red) obtained by averaging over 2000 neighbors for each Fourier mode.

5.2 Surrogate Assisted Analysis of Empirical Time Series

5.2.1 A Few Empirical Time Series

Let us first introduce the experimental time series that will accompany us through the next section.

Dow Jones Industrial Average

A white leptokurtic time series stemming from a heavily nonlinear and complex system is the series of the logarithmic daily returns of the Dow Jones Industrial Average [Williamson, 2015]. This time series has been acquired by taking the differences between each decadic logarithm of daily closing prices from 26$^{\text{th}}$ of May 1896 until

23^{rd} of October 2014, resulting in $N = 32222$ time steps[2]. This time series will be referred to as *DJ*.

Tailored Nonlinearities
The next time series example is not experimentally obtained but has been synthesized to match all fundamental scaling properties of the PDF of the DJ data set. This was achieved by imposing a set of six linear correlations on the Fourier phases [Räth and Laut, 2015]. While the original time series has $15 \cdot 10^5$ time steps, only a shorter version that is cropped to the exact length N of DJ is used in the current analysis. The method Räth and Laut proposed to construct this data set can in some sense be regarded as the inverse of the analysis method proposed in this work. Instead of tracing phase correlations in nonlinear data, the authors succeeded in reproducing leptokurtic PDFs with scale invariant properties by correlating the phases of Gaussian white noise. Not only static nonlinearities have hereby been produced but also events that appear as bursts. In this section, it is demonstrated that phase walk analysis can confirm this and further find differences between the time series and its prototype DJ. This time series is called *TN*.

Wind Acceleration
A time series of wind velocities collected at an Atlantic offshore wind turbine [National Renewable Energy Laboratory, 2014] serves us as a leptokurtic example that shows some relevant linear properties. To make the time series more comparable to the previous two examples, it is convenient to center it by taking the differences between the time steps and to also crop it to the length of DJ. As a result, the time series reaches from January, 1^{st}, 2004, 00:10 until Juli, 10^{th}, 2004, 18:20. The difference between two consecutive velocities is the change in velocities and hence, the wind acceleration (*WA*). The power spectrum of this data set drops towards higher frequencies. However, this characteristic appears only as a noisy trend and cannot clearly be recognized as a power law decay, which would be a typical consequence of turbulent behavior [Frisch, 1995]. This is due to rather strong under-sampling of the data. Turbulent motion of air shows relevant effects down to time scales of a few milliseconds[3], but the present data has only been recorded with a sampling period of 10 minutes. However, the SRT enables an identification of nonlinearities in the data set with outstanding significance, which is shown in the remainder of this chapter. Fig. 5.2 shows all time series and the corresponding power spectra.

To obtain statistically reliable results in the following tests, one has to first define some null hypothesis. For this, the surrogate algorithms introduced in Section 4.8

[2] $x_{DJ}(t) = \log_{10}(p(t)) - \log_{10}(p(t-1))$, where $p(t)$ is the closing price on day t.

[3] The Kolmogorov time scale can be approximated as $\tau_\eta = \sqrt{\nu/\epsilon} = \sqrt{\nu L/\langle u \rangle^3} = \sqrt{1.5 \cdot 10^{-5} m/s \cdot 10 km/(8.7 m/s)^3} = 15 ms$. Here, ν is the kinematic viscosity of air, $\langle u \rangle$ is the velocity mean and L is the typical length scale of the system. The latter is hard to estimate for an outside environment but even if we choose $L = 10000 km \approx d_{EARTH}$, τ_η does not exceed $500 ms$.

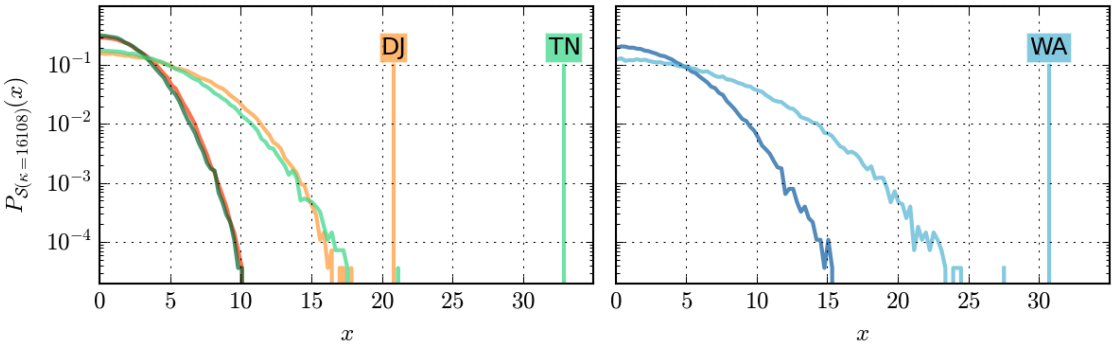

Figure 5.3: Left: PDFs of the SRT results (null distributions) for the DJ and the TN data sets. Right: The results for the WA data set and its surrogates.
The results for the different time series are grouped by their colors (orange for DJ, green for TN and blue for WA), while the shuffled surrogates are darker than the IAAFT surrogates. Additional to the PDFs, the vertical lines labeled by the names indicate the outcomes for the original data sets. IAAFT surrogates tend to produce much wider distributions than the shuffled versions.

are utilized. For each of the time series, one set of 10^5 shuffled and one set of 10^5 IAAFT surrogates have been generated. The former are especially suited for the white time series (DJ and TN) and the latter for the data sets with possible linear features (WA). Fig. 5.3 shows the empirical PDFs of $\mathcal{S}(\kappa = 16108)$ for the surrogate data sets and for comparison the results of the unaltered time series. Let us first discuss the results for the white time series DJ and TN.
As already mentioned before, TN has been tailored to exactly match the PDF of its prototype DJ and hence, it is not surprising to find their null distributions very similarly lying upon each other. The results for the time series themselves on the other hand differ vastly ($\mathcal{S}_{DJ} = 20.9$ and $\mathcal{S}_{TN} = 32.9$). This implies that although the static nonlinearities have been reproduced very accurately, the dynamic nonlinearities of both data sets still deviate by a serious amount. TN even carries nonlinear features that are much more significant, at least when measured with the SRT.
Interesting to observe is further that the distributions associated with the IAAFT surrogates are completely distinct from those associated with the shuffled surrogates. This can only be explained by assuming that IAAFT surrogates carry nonlinearities that are not solely induced by the PDF. In the next section, this issue will be discussed in further detail.
In any case however, the time series can be attested to bear dynamic nonlinearities with a significance of at least one in 10^6, most likely even orders of magnitude higher. Tab. 5.1 summarizes the significances measured in standard deviations. Note that this is actually not a proper way of telling the significances in the current case, since the results are not distributed normally. In many publications though, multiples of standard deviations are routinely used to quantify the significances of various nonlinearity test even if only a few as maybe one hundred surrogates have been

Time Series	Surrogate	$\mathcal{S}(\kappa = 16108)$	NLPE
DJ	shuffled	13.7σ, 20.4σ 14.4σ	35.3σ, 35.2σ, 37.0σ
DJ	IAAFT	7.4σ, 7.0σ, 8.1σ	39.6σ, 35.0σ, 30.5σ
TN	shuffled	21.9σ, 22.1σ, 22.4σ	45.5σ, 52.6σ, 48.6σ
TN	IAAFT	13.9σ, 12.6σ, 12.5σ	47.3σ, 51.2σ, 45.8σ
WA	shuffled	14.0σ, 13.9σ, 14.0σ	44.0σ, 28.4σ, 43.6σ
WA	IAAFT	10.5σ, 8.6σ, 8.6σ	32.8σ, 32.8σ, 33.8σ

Table 5.1: Significances for dynamic nonlinearities present in the empirical time series. Each field contains three results from evaluations with 10 surrogates.

created[4]. The significances should in any way suffice for most purposes and can easily compete with many established measures like those mentioned in Section 2.2.3.

For comparison, Tab. 5.1 also contains results for the NLPE. The parameters for the analysis of the wind data were selected to match those in a publication by Ragwitz and Kantz [2000], since their object of study has been a time series of near-surface wind velocities, very comparable to WA. Ragwitz and Kantz embedded a one-dimensional time series into a $d = 20$ dimensional phase space.
For the NLPE analysis of the Dow-Jones data the parameters were borrowed from Small and Tse [2003] since they studied the very same time series. In their analysis, they used an embedding dimension of $d = 8$ but unfortunately an unmentioned number of nearest neighbors. A probably good choice, as Sugihara and May suggest, is given by $k = d + 1 = 9$. While Small and Tse reached a maximal confidence of 98%, the current implementation revealed $\sim 35\sigma$. Phase walk analysis on the other hand performed comparably well with up to $\sim 20\sigma$[5]. Each entry is based on only ten surrogates, since the NLPE is computationally extremely intense. I.e., to compute the NLPE, one has to find k nearest neighbors ($k = 50$ for WA) for every one of the N data points in the set (see also Section 2.2.3.5). The most efficient k-nearest-neighbor algorithms known to the author scale in runtime with $\mathcal{O}(d \cdot k \cdot N)$. Next, one has to average over the trajectories of all of those neighbors (one average per dimension) and compare this average to the real trajectory of the selected data point. This has to be done for every N data points. The computational runtime hence turns out to be approximately proportional to $\mathcal{O}(d \cdot k \cdot N^2)$, neglecting the averaging processes.

[4]The significance in multiples of standard deviations is commonly obtained by dividing the absolute difference between the test result $\mathfrak{R}$ of the time series and the mean of the null distribution μ_{ND} by the standard deviation of the null distribution σ_{ND}: $|\mu_{ND} - \mathfrak{R}|/\sigma_{ND}$. This can lead to completely false results if the null distribution is not Gaussian, which is indeed generally to be expected. Moreover, the smaller the cardinality of the set of surrogates, the more questionable the result becomes.
Note that Tab. 5.1 also relies on this technique. Here, also the scattering of the significances takes effect.

[5]Both significances indicate extremely unlikely events. For reference some corresponding likelihoods: $7\sigma \mathrel{\widehat{=}} 10^{-12}$, $14\sigma \mathrel{\widehat{=}} 10^{-44}$, $20\sigma \mathrel{\widehat{=}} 10^{-89}$, $35\sigma \mathrel{\widehat{=}} 10^{-268}$.

Computing $\mathcal{S}(\kappa = 16108)$ on the other hand requires a Fourier Transform and one averaging process which results in an approximate runtime scaling of $\mathcal{O}(Nlog(N))$, also neglecting the averaging. For the analysis of the three example time series, the number of feasible calculations of $\mathcal{S}$ exceeded the number of NLPE calculations by four orders of magnitude. Note that most of the powerful, advanced measures for nonlinearities in time series rely on embedding and clustering of data points (NLPE, multifractal dimensions, Lyapunov exponent, network based measures), leading to a roughly equal scaling in computational effort. Furthermore, there is no distinction between linear and nonlinear properties in any of the methods known to us. This is an important feature, since it allows for studying both classes of properties separately, and hence for encircling certain features with much greater precision. The runtime gain is not only convenient for data analysts but enables greater precision in the result[6] and utilization of the method in time critical applications.

The analysis for WA produced equally sufficient significances in both the shuffled and IAAFT comparison. Surprisingly though, the ratio of the standard deviations of the PDF of the shuffled surrogates to that of the IAAFT surrogates is approximately equal to the same ratio for the Dow Jones time series.

$$\frac{\sigma_{\mathcal{S}_{DJ_{shuffled}}}}{\sigma_{\mathcal{S}_{DJ_{IAAFT}}}} \approx 0.63, \quad \frac{\sigma_{\mathcal{S}_{WA_{shuffled}}}}{\sigma_{\mathcal{S}_{WA_{IAAFT}}}} \approx 0.65 \tag{5.3}$$

This may be taken as a rather unexpected result since unlike DJ, WA has substantial linear features, which are destroyed by shuffling the data. Thus, the ratio for WA should possibly be smaller compared to the ratio for DJ, which is not the case.

In the next chapter we will have a look at the nonlinear effects solely induced by the IAAFT algorithm.

5.3 IAAFT-induced Nonlinearities

As already mentioned in the previous section and actually visible in Fig. 5.3, IAAFT surrogates carry nonlinearities that can neither be explained by the PDF of their prototype nor by linear properties of it. To verify this, 10000 shuffled surrogates for independent and identically distributed leptokurtic noise are compared with 10000 corresponding IAAFT surrogates. The number of time steps of the prototype noise time series is 10000 as well. Fig. 5.4 evidently exposes IAAFT-induced nonlinearities, not present in the shuffled alternatives. As Dolan and Spano [2001] argue, it may therefore be a preferred procedure to reproduce the power spectrum not exactly, but only statistically instead. Since shuffling remains a satisfying surrogate generation strategy for at least DJ and TN, however further comparisons with other surrogates have not been included in the previous evaluations of the presented data and measures.

[6]Comparing the null distributions in Fig. 5.3 to the significances in Tab. 5.1 reveals that the significances are actually less than indicated in the table.

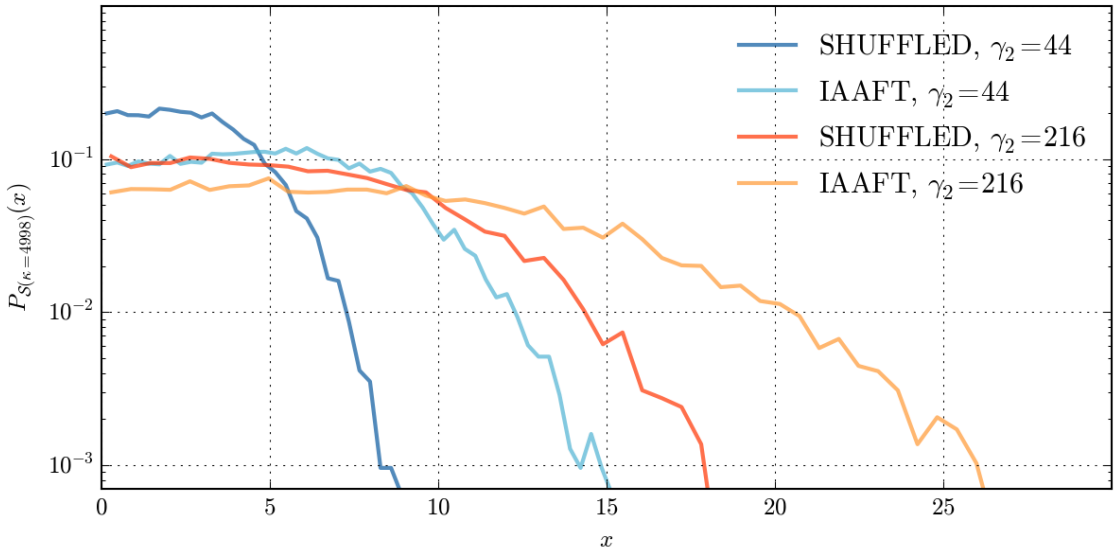

Figure 5.4: PDF of SRT results for surrogates of leptokurtic noise. The blue PDFs correspond to noise time series with a kurtosis of $\gamma_2 = 44$ and the reddish to noise with $\gamma_2 = 216$. In each case the IAAFT surrogates results differ from the results for shuffled surrogates tremendously.

Moreover, as the IAAFT algorithm induces false nonlinearities, it may yield misguided but also even stronger null hypothesis. Thus, the test significances derived for WA (see Tab. 5.1 or Fig. 5.3) in the IAAFT assisted analysis might probably even be understated.

5.4 Rotational Analysis of Empirical Time Series

In Section 4.6 the concept of time series rotating has already been introduced. It will now be applied to the three example time series to derive their rotation maps (Fig. 5.5). $\mathcal{S}(\kappa)$ could in any case be increased at least 11%.
All maps basically show two broad and asymmetric peaks separated by well pronounced valleys. The positions of those can sometimes be used to hint to positions of bursts or emergent events in the time series. In Section 4.1, we already saw that fake wraps are caused if the dominant delta-peak sits in the second half of the time series, since the phase difference between two consecutive Fourier modes exceeds π. If it sits right in the middle of the time series, this difference or phase rotation is exactly equal to π, which causes the unwrapping mechanism to stochastically interpret the differences alternatively as clock- and counterclockwise. Hence, the unwrapped phase differences fluctuate between $-\pi$ and π, leading to a net rotation of 0. This effect manifests itself as a relatively steep valley in the rotation map if one especially well defined peak or bursty event influences the time series. Fig. 5.6 illustrates this incident for TN, where it is best visible among the three example

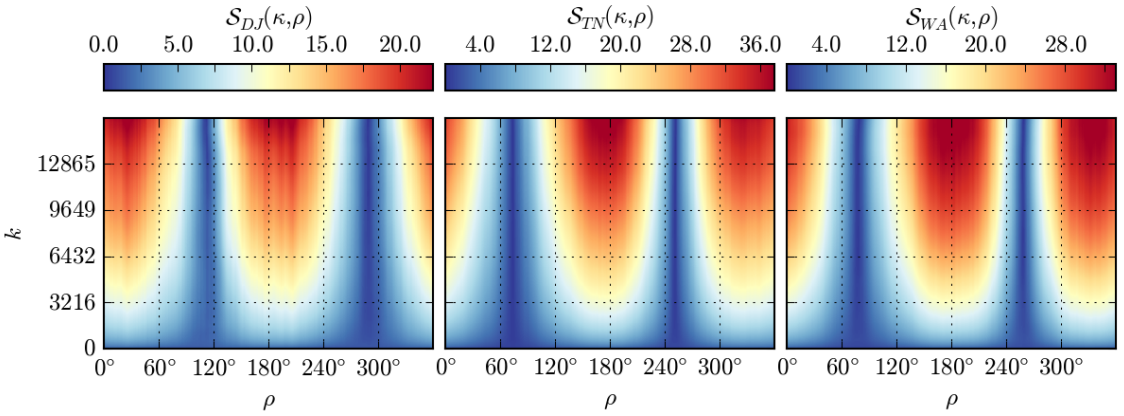

Figure 5.5: SRT results for different rotation angles. The maximal values increase to $\mathcal{S} = 23.2$ for DJ at a rotation angle of $\tau = 2300 \mathrel{\widehat{=}} 25.7°$, to $\mathcal{S} = 39.2$ for TN at a rotation angle of $\tau = 15151 \mathrel{\widehat{=}} 169.6°$ and to $\mathcal{S} = 34.5$ for WA at a rotation angle of $\tau = 16251 \mathrel{\widehat{=}} 181.9°$. This corresponds to increases by 11.0% (DJ), 18.7% (TN) and 12.4% (WA).

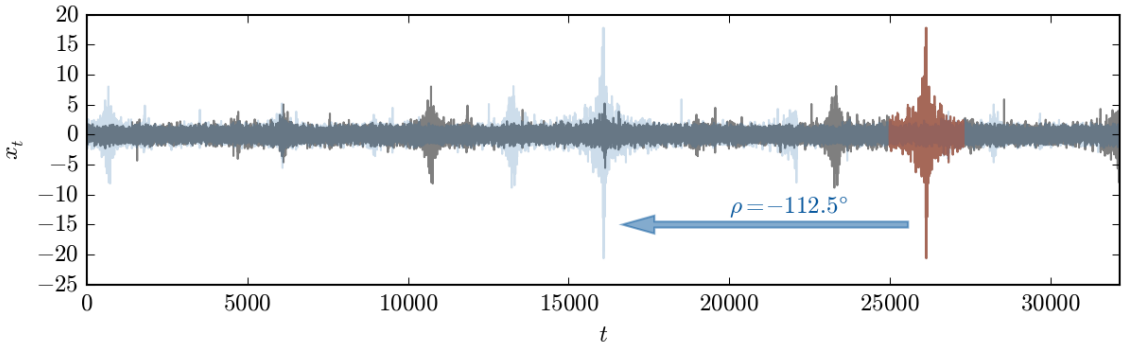

Figure 5.6: The time series TN (gray). A rotation by $\rho = -112.5°$ shifts the highlighted bursty region (red) into the middle of the time series, causing the SRT results to become minimal (see Fig. 5.5 middle).

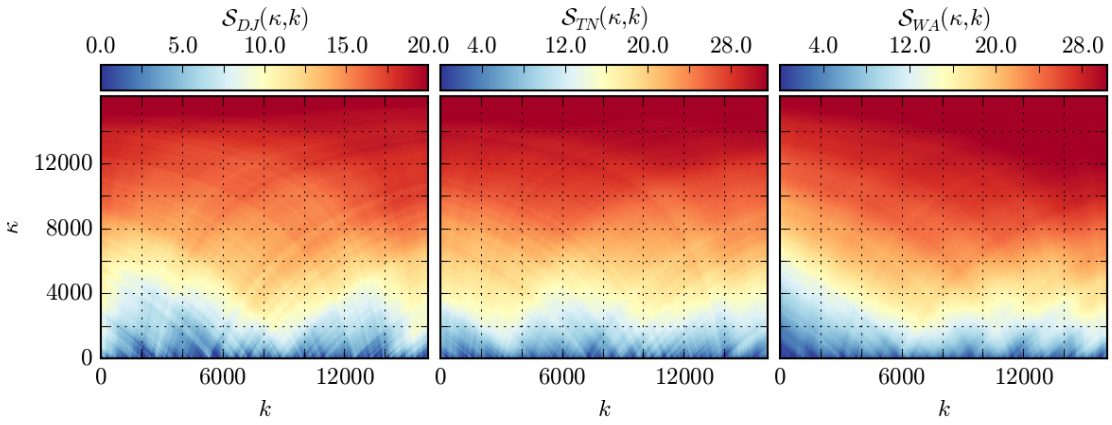

Figure 5.7: SR-maps for the three time series DJ, TN and WA. All of them increase quite homogeneously to greater values of κ and show no significant frequency dependent irregularities.

time series. The rotation angle has been selected by the position of the right hand minimum in the map for TN in Fig. 5.5 ($-112.5° \mathrel{\widehat{=}} 247.5°$).
These minima can of course also have other reasons. For example, if the time series is rotated such that it becomes somehow symmetric, the slopes induced by peaks or bursty events can cancel out. This can be explained by stressing the same argument as before: From Eq. 3.4 it follows that peaks in the first half of the time series cause phase slopes below π, while peaks in the second half cause slopes greater than π. If the latter is the case, they get wrapped, that is, decreased by 2π and hence negative. Thus, peaks in the second half cause the exact opposite slope than peaks in the first half. If in both parts comparable peaks exist, they may cancel out.
Further and more complicated reasons for the emergence of the characteristic structure in the rotation maps may exist but are not discussed here, since no deeper insight would be gained at this point.

5.5 SR-Maps of Empirical Time Series

In Section 4.5, another way to depict SRT results was discussed, that allows for identifying frequency bands, and hence relevant time scales of nonlinear phenomena. Applied to the experimental time series, the maps illustrated in Fig. 5.7 appear. None of the three maps shows significant k-dependent irregularities. Instead, $\mathcal{S}(\kappa, k)$ increases quite homogeneously over the whole frequency band. This suggests that all time series were subject to nonlinear influence on all time scales, which agrees with what one would expect:
DJ is a financial time series and underlies myriads of different dynamics happening on all time scales from Flash Crashes, lasting several minutes [Phillips, 2010] to century-spanning economic growth periods.
TN was synthesized by correlating all its phases. Therefore, obviously all frequency

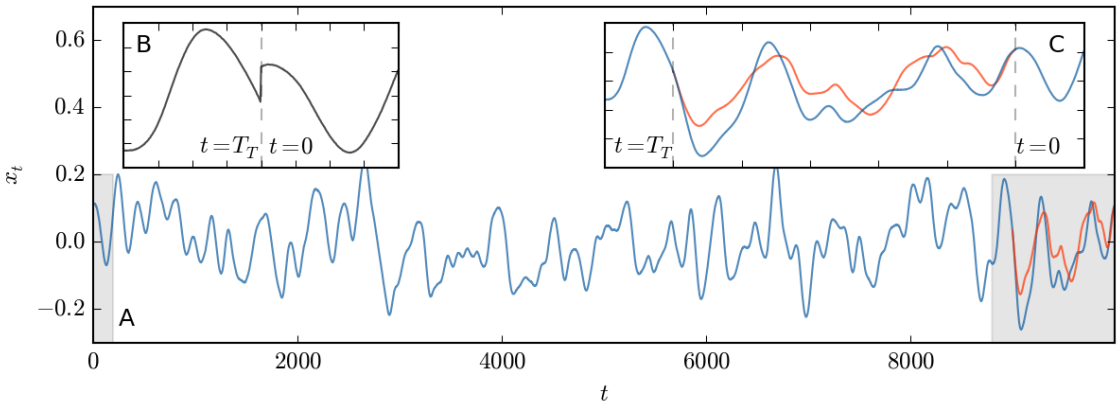

Figure 5.8: The linear stochastic process is plotted in blue and the inpainted link in red. Box C shows a zoom into the gray region of A. In Box B the joint between the last and the first time step of the trimmed linear process is shown.

bands are affected as well.
WA contains outdoor wind acceleration data over a period of more than eight months. It is reasonable to assume fully developed turbulent air flow at the location where the data was recorded and hence, there should have appeared eddies on technically every length and time scale [Kolmogorov, 1941b,a], maybe except for the time scales of multiple weeks or months. This region however is presumably also subject to complex dynamical influence by seasonal changes. Note that since amplitudes and phases are decoupled in Fourier space, turbulent influence on weak modes has the same impact on the phase statistics as it has on strong modes. Consequently, also WA should carry phase correlations over the whole frequency band, which is indeed true as Fig. 5.7 reveals.

5.6 Inpainting to Remove Edge Effects

As already brought up in Section 4.7, it might be interesting to utilize the inpainting technique not only to remove spurious influence of discontinuities at the time series edges on the power spectrum (the linear properties), but also on the Fourier phases. Let us therefore investigate a linear stochastic process with dominating low frequency modes that has been constructed by low-pass-filtering a series of Gaussian random variables (Fig. 5.8). Constructing it this way also ensures that the process is initially free of edge effects, since the phases remain unaltered when applying the filter.

The time series is then trimmed to simulate a stop of recording. Hence, the edges are not smoothly closed anymore but can only be joined by a harsh discontinuity (see Fig. 5.8 B). Since this highly nonlinear event is located at the temporal position $t = 0 \mathrel{\widehat{=}} t = T_T$ (T_T is the number of time steps of the trimmed version), most phases become 0 by tendency and the phase walk is primarily centered (see Eq. 3.4 for $\tau_j = 0$). To avoid this effect in the phase walk analysis, the series has to be rotated.

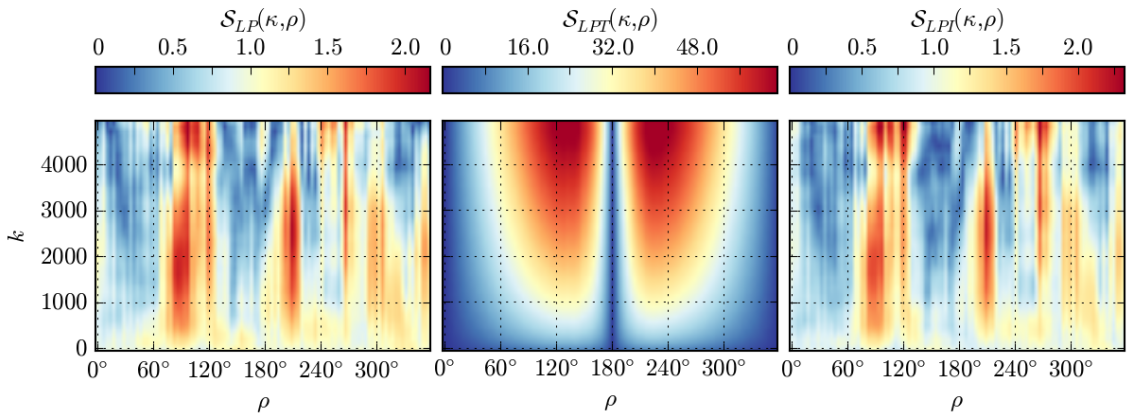

Figure 5.9: SR-maps for the linear process (left), the trimmed linear process (mid) and the inpainted linear process (right). While the original and the inpainted variant show very similar patterns, the trimmed version is completely dominated by the edge effects. $\mathcal{S}_{LPT}(\kappa)$ reaches even values of ~ 60, which exceeds any outcome of the previous analysis.

To convince the reader that this really holds true, the rotation maps for both the untrimmed and trimmed time series are shown in Fig. 5.9: for a rotation angle $\rho = 0°$, $\mathcal{S}(\kappa)$ is basically equal to 0 for the trimmed version. Two extremely well defined peaks with a steep valley in between them (see Sec. 5.4 for a detailed explanation) can also be recognized in this map and no significant feature at all in the map of the untrimmed process. Hence, the rough transition at the edges of the time series obviously causes indeed striking nonlinear effects directly observable in Fourier space. Fig. 5.10 also shows the power spectra of both versions. Trimming the time series even impacts the linear properties by lifting non-present Fourier modes into a relevant regime.

The reader might have gained a gloomy impression about the consequences of edge effects by now and maybe even feels motivated to add a slick solution to this problem by inpainting a link between the two edges. To do so, one can proceed as described in Section 4.7.
Fig. 5.8 depicts the original time series and the one with the inpainted link. For removing artifacts a very weak noise floor has further been added to both, the original and the inpainted time series[7]. The inserted segment clings neatly to the open edges of the trimmed time series and also seems to agree quite well with its linear properties, as can be seen in Fig. 5.10 (middle).

This example demonstrates that inpainting might state a powerful alternative to window functions. While the latter modifies the time series itself, inpainting leaves it unaffected while basically solving the problem. A deeper analysis would certainly be of great interest for data- as well as signal analysis.

[7]Also the trimmed version carries this noise floor of course.

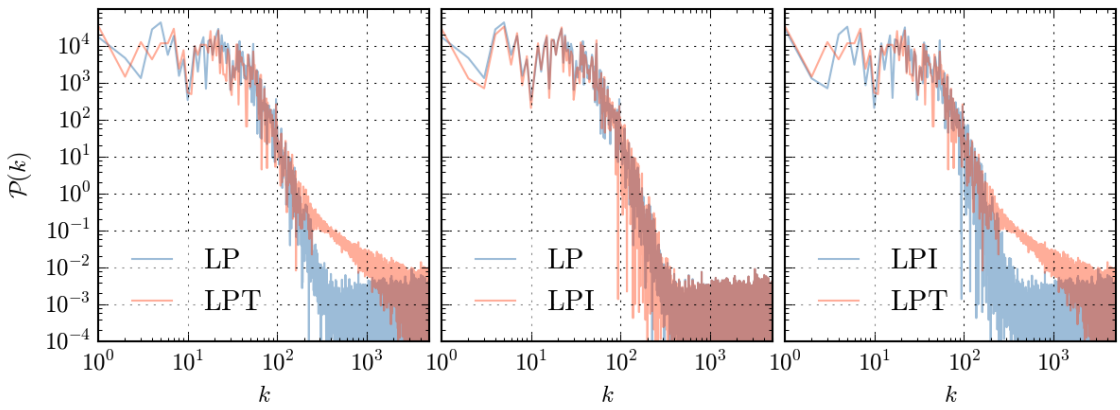

Figure 5.10: Power spectra of the linear process (LP), the inpainted linear process (LPI) and the trimmed linear process (LPT). To see how well they match, each picture shows two of them overlaid. The original and the inpainted version comply quite good, while the spectrum of the trimmed time series has numerous elevated modes between $k \approx 200$ and $k \approx 3000$. For better comparability, the power spectrum of LPT has been stretched to the other spectra's length. k therefore constantly deviates by +10% for LPT.

5.7 Inpainting to Identify Dominant Regions

In this section, another application of inpainting that is especially relevant for time series with bursty or peaky passages will be encountered. Consecutive regions of the time series are successively masked and filled with inpainted segments. For each position, a SRT result is recorded. All time series have first been rotated to the position of maximum test response (see the description of Fig. 5.5 for the actual angles). Fig. 5.11 illustrates the result. Inpainted segments in the first half of the data cause $\mathcal{S}$ to drop by tendency and vice versa for the second half. This indicates that the dominating nonlinear events are located in the first part and can be explained the following way.

Nonlinear events in the first half result in phase slopes greater than 0, since they get wrapped correctly, while events in the second half cause negative slopes. High SRT results can stem from both steep positive or negative slopes. If $\mathcal{S}$ decreases when passages from the first half are removed, it means that the absolute slope is reduced when positive contributions are taken out. Hence, the phase walk must have had an overall positive slope and therefore dominating nonlinearities in the first part. This also suggests that $\mathcal{S}$ should increase if nonlinear events in the second half are removed, since they contribute negatively. That is exactly what can be observed. To confirm this argument, the same plots are given for all time series rotated by 180° in Appendix B.1. This basically exchanges the front and the rear part (moving the dominant event to the opposite half) and causes $\mathcal{S}$ to acquire the opposite trend. Let us now discuss all time series separately in detail.

DJ (top): Two regions of weighty nonlinear behavior at $t \approx 13000$ and $t \approx 27500$ can easily be identified. The first event reaches from ~ 1929 to ~ 1940 – the time of

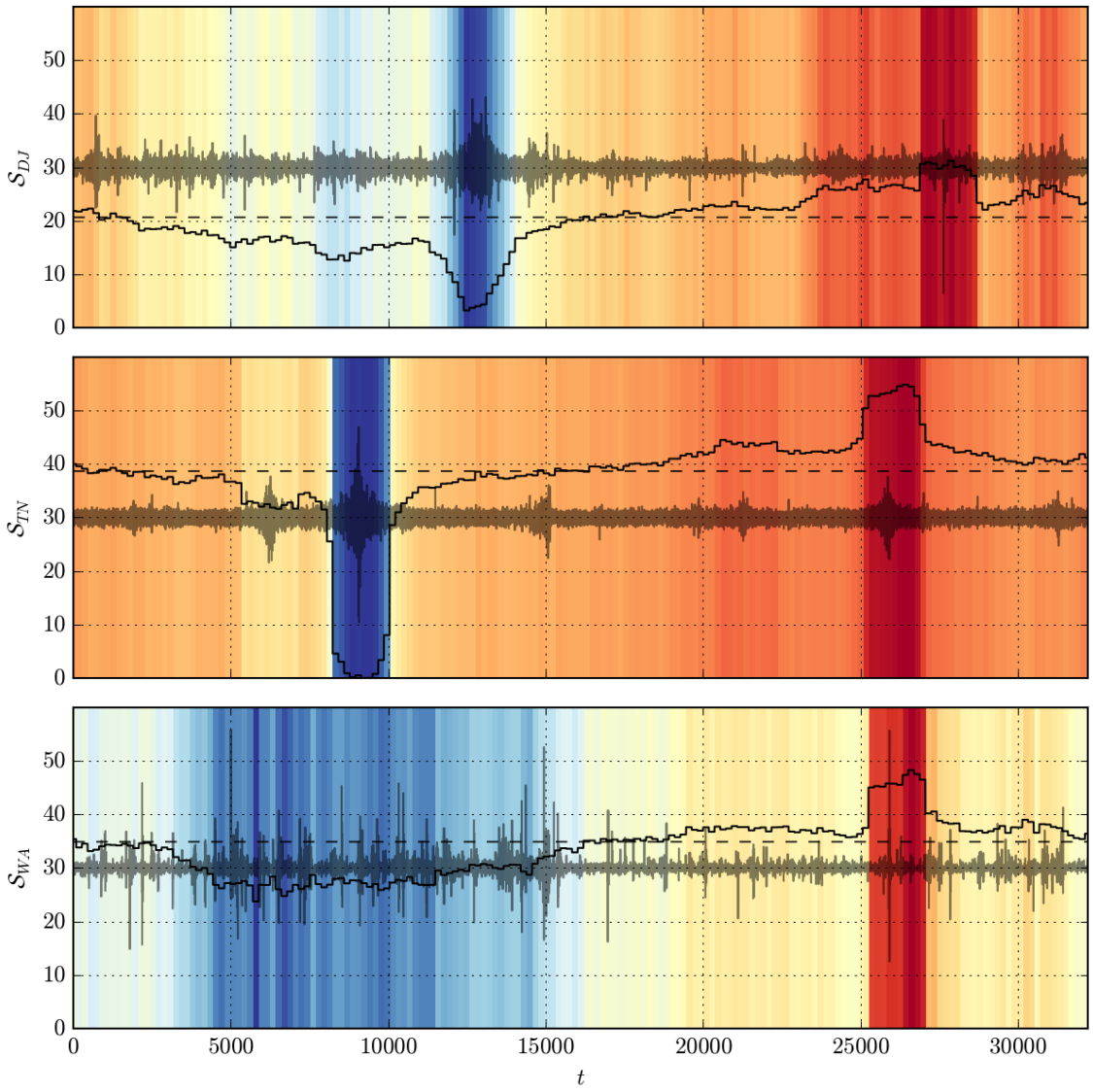

Figure 5.11: SRT results for time series with inpainted segments. The solid black curve in each graph shows the result $\mathcal{S}(\kappa = 16108)$ of the SRT-test of the time series when a region of width $= 1800$ at the corresponding position t was replaced by an inpainted segment. $\mathcal{S}(\kappa = 16108)$ of the unaltered time series is also indicated as dashed black lines. The background redundantly encodes this value: blue corresponds to a drop and red to an increase in $\mathcal{S}(\kappa = 16108)$. The grayish curves are the time series in arbitrary units.

the Great Depression. The second event can be identified as the Black Monday on October 19, 1987.
TN (mid): Also here, two passages ($t \approx 9000$ and $t \approx 26000$) essentially govern the trend of $\mathcal{S}$. Inpainting the first event causes the SRT-result even to completely collapse. This may have its reason in the symmetry of the residual time series: as previously explained, similar nonlinearities in the front and rear part can cancel out in the SRT result. This is also why swapping the second event by an inpainted segment increases the SRT result.
WA (bottom): This curve behaves somehow different than the previous two. One recognizes a widespread decrease of $\mathcal{S}$ in the first half for $t \approx 4000 - 16000$, corresponding to the time from early May to Juli – spring to summer, when the weather is more turbulent in the northern hemisphere. A second single peak impacts at $t \approx 26000$, which is in late February – maybe squall.
These results indicate that inpainting assisted phase walk analysis states an extremely powerful new tool for nonlinear data analysis. The technique is not only able to identify nonlinearities at all, but to precisely locate them in the time series.

5.8 Inpainting to Resolve Nonlinearities in Symmetric Time Series

The careful reader might already have noticed that symmetries in time series state a crucial issue for SRT based phase walk analysis, because their effect on the Fourier phases might destructively interfere (see Section 5.7). A time series that gives a good example of this effect is TN, which is highly symmetric in its full length $N_{TN} = 150000$. The SRT results reach only maximal values of $\mathcal{S}(\kappa) \approx 0.9$ when applied to the unrotated time series. Fig. 5.12 shows the results for inpainting assisted analysis. Inpainting increases $\mathcal{S}$ to up to approximately 23.3 for the most influential regions and to values over ~ 5 for at least 4 events. Note that one of the most striking events in the time series happens to be located at the very center and thus, stays without effecting the SRT at all (see Section 5.4 for a detailed explanation). To access this event anyhow would for example be possible by slightly rotating the time series. Since this is not the aim of this chapter however, it is just left as a remark here.

5.9 Nonlinearities in Turbulent Particle Trajectories

As one last example, SR-maps have been computed for particle accelerations in a dusty plasma.

Complex or dusty plasmas are low temperature plasmas with embedded micrometer-

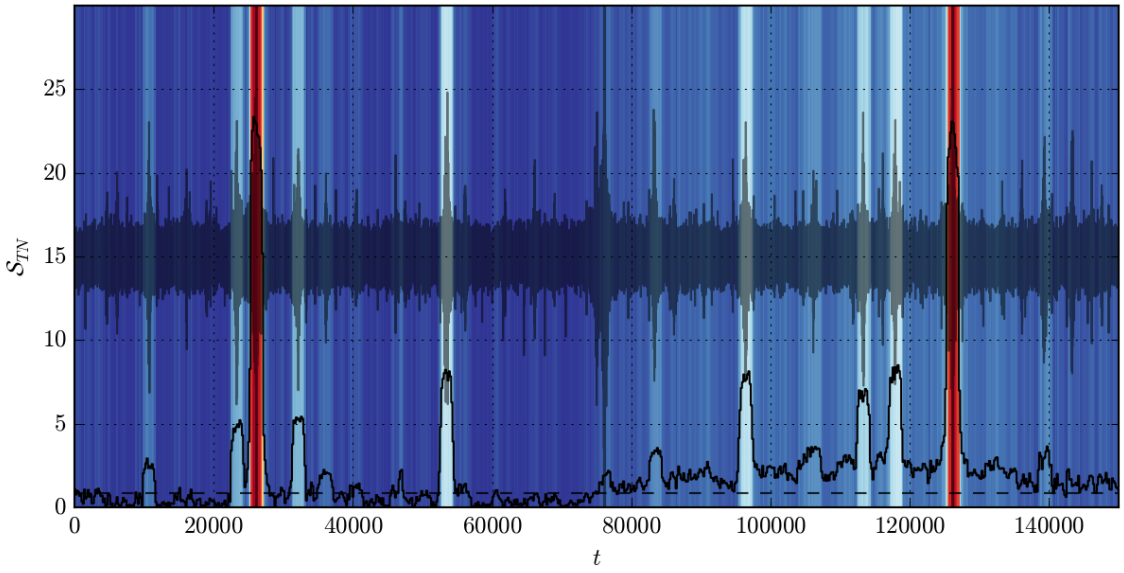

Figure 5.12: Inpainting assisted SRT of the full-length TN. TN itself is visible as a gray shadow. The solid black curve is the series of SRT results dependent on the position of the inpainted segments of width 1800 and the dashed line indicates the result for the unaltered time series. In addition the position-dependent results are redundantly color-coded in the background: blue corresponds to a drop and red to an increase in $\mathcal{S}(\kappa)$.

sized particles [Thomas et al., 1994; Fortov et al., 2005; Ivlev et al., 2012]. Because of the higher mobility of the electrons in an ionized gas, the particles in general become negatively charged. Together with the resulting Debye sheath this produces a Yukawa-like pair-potential over which they interact. As a result, dusty plasmas can exist in all of the three classical phase states, solid, liquid and gaseous, and further display many complex phenomena, like e.g. melting and recrystallization [Thomas and Morfill, 1996; Knapek, 2011], wave phenomena [Merlino et al., 1998; Nosenko et al., 2002], or self-organization [Kong et al., 2011; Wörner et al., 2012]. Since the inter-particle distances are on the range of approximately $100 - 500\mu m$, the particle clouds can easily be observed when illuminated by a laser. Therefore, they are ideally suited as model systems to study generic phenomena like those just mentioned.
In huge three-dimensional particle clouds, also vortex-like streams can sometimes be observed [Nefedov et al., 2003; Morfill et al., 2004; Heidemann et al., 2011]. In a recent publication by Schwabe et al. [2014] a simulation of a two-dimensional dusty plasma sheet, modeled after the PK-3 Plus laboratory [Thomas et al., 2008], has been used to show that even turbulent characteristics develop in those vortices. In this last chapter, these simulation results are investigated by phase walk analysis to classify different areas in the vortices.

7100 particles of diameter $3.14\mu m$, mass $3.1 \cdot 10^{-14} kg$ and a charge of $-3481e$ were simulated in an environment of argon plasma with a pressure of $10Pa$, a neutral gas temperature of $300K$, an electron temperature of $2.4eV$ and an ion number density

of $3.4 \cdot 10^{14} m^{-3}$. The frames were grabbed at a sample period of $10ms$ over a runtime of $60s$, resulting in $N = 6000$ time steps.
The time series, used for the SRT, are the accelerations in y-direction that were calculated by simply taking the differences of the differences of the coordinates in real space[8]. Fig. 5.13 (top) shows 100 randomly picked trajectories (gray) of the data set: two counter-rotating vortices (counterclockwise rotation of the upper and clockwise rotation of the lower vortex) are formed. In the center of each vortex mostly stable and steady rotations occur, whereas particles that travel at the edge of the particle cloud (at the *void* – the region located at $x \approx 0 - 7mm$, $y \approx 8 - 12mm$, and at the outer edges) are subject to irregular accelerations that presumably occur whenever they leave and enter their rather homogeneous particle dominated neighborhood. For four representative trajectories of each area the SR-maps were computed and plotted as well in Fig. 5.14. As expected by the previous argument, the unstable trajectories carry significant frequency dependent anomalies, while the stable rotations do not show any indicative features. One can observe that especially the lower or the higher frequency regions are suspicious. The former might be explained by the overall shape of the unstable particle trajectories, which deviates clearly from a harmonic oscillation, compared to the stable rotations. The latter do probably result from the transitions through the various cloud regions happening on short time scales. Here, especially the regions at ($x \approx 8mm$, $y \approx 10mm$), ($x \approx 22mm$, $y \approx 10mm$), ($x \approx 4mm$, $y \approx 14mm$) and ($x \approx 4mm$, $y \approx 6mm$) are addressed, where the trajectories describe comparably sharp bends.

The result demonstrates how particle trajectories can be allocated to different regions by merely scanning the Fourier phases for some distinctive features.
It also supports once more that phase walk analysis is applicable to most different fields of physics and other sciences. The current example led to significant results, although the time series do not even show leptokurtic probability distributions. This indicates that Fourier phase-based analysis techniques may most likely find applications for data of other characteristics as well.

[8] $a(t) = (v(t) - v(t - 10ms))/10ms = [(y(t) - y(t - 10ms)) - (y(t - 10ms) - y(t - 20ms))]/(10ms)^2$.

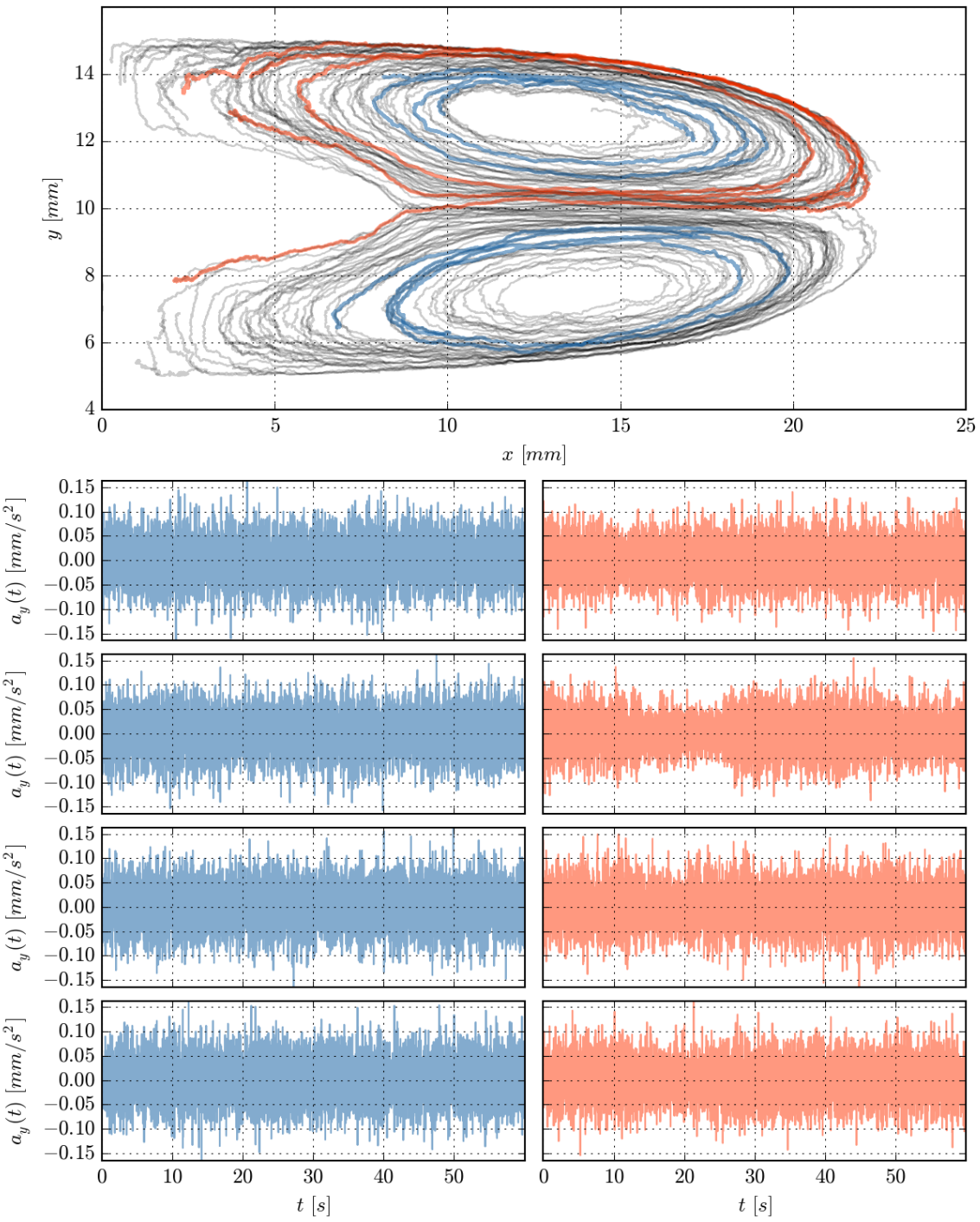

Figure 5.13: Top: 100 randomly picked particle trajectories (gray) to visualize the system, four trajectories from the inner region of the vortices (blue) and four trajectories from regions near the void and / or the outer edges of the particle cloud (red). The left column below shows the acceleration in y-direction of the four stable oscillations (blue) and the right column the acceleration of the unstable trajectories (red). The same figure for the x-accelerations can be found in Appendix B.2.

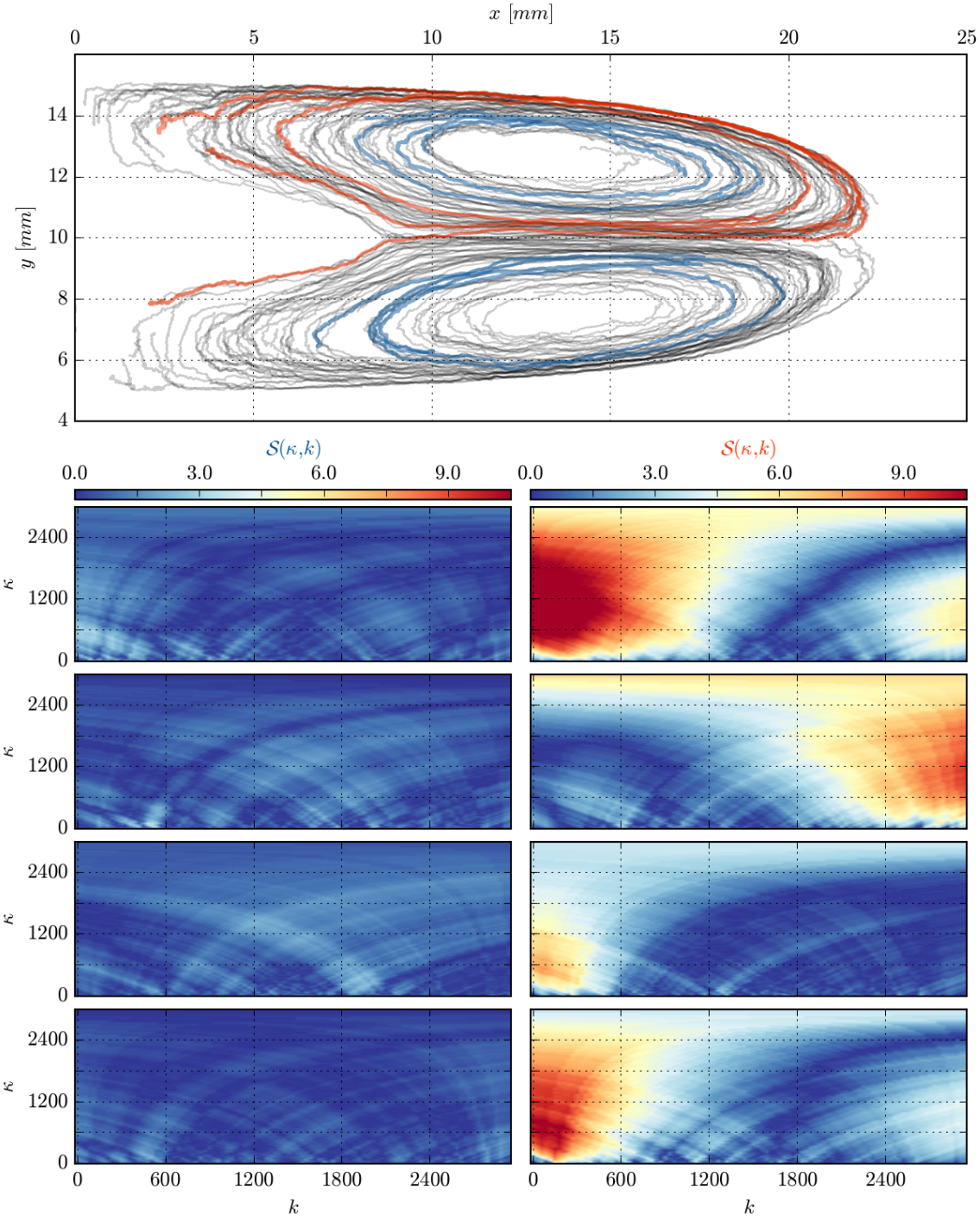

Figure 5.14: Top: 100 randomly picked particle trajectories (gray) to visualize the system, four trajectories from the inner region of the vortices (blue) and four trajectories from regions near the void and / or the outer edges of the particle cloud (red). The latter show well-marked phase anomalies in the SRT results, while the stable vortex rotations are rather inconspicuous by tendency. Below: The left column shows the SR-maps that correspond to the the y-accelerations of the blue trajectories in the top figure and the right column those corresponding to the red trajectories. Well observable, the stable rotations (blue, left) cause no significant deviations from the random walk hypothesis, while the outer trajectories (red, right) show large frequency dependent aberrations. The same figure for the x-accelerations can be found in Appendix B.3.

Chapter 6

Conclusions

Let us briefly summarize what has been encountered in the course of this work.
In the first part, it was argued that, since all nonlinear time series properties live in the Fourier phases, a measure, able to quantify these features, would permit a whole new class of analysis techniques selectively sensitive to nonlinear features.
An analytic description of the implications of leptokurtosis on the Fourier phases followed then to derive a methodology that can capture various anomalies within them. A few simple examples helped here to get familiar with the methods and to characterize them. The tools (SRT, SR-maps and the rotational maps) turned out to be excellently suited for leptokurtic data. This enabled the discovery and quantification of a statistical relationship between kurtosis and the Fourier phases.
Next, a surrogate supported analysis was used to compare the test significances for dynamic nonlinearities in empirical time series with a very reliable and commonly used measure, the Nonlinear Prediction Error (NLPE). It turned out that phase walk analysis performed with minor, yet more reliable and absolutely sufficient significance. I.e., in the analysis of the time series with tailored nonlinearities, the SRT significance reached $\sim 22\sigma$, while it reached $\sim 48\sigma$ for the NLPE. On the other hand, the SRT results formed a smooth null distribution that spanned over five orders of magnitude, while only ten NLPE results could be obtained in the same time due to the high computational effort, intrinsic to delay-time-embedding based measures. Apart from this, the minimal significance reached by the SRT in any of the presented tests was $\sim 7\sigma$, which corresponds to approximately one in 10^{12} events.
Following this, a comparison between iterated amplitude adjusted Fourier-transformed (IAAFT) and shuffled surrogates of independent and identically distributed random variables revealed significant dynamic nonlinearities induced by the IAAFT algorithm.
The chapter continued with applying more sophisticated variants of the SRT to the data sets. Rotating the time series led to an improvement of the significances and allowed for localizing especially nonlinear events in the time series. Furthermore, SR-maps showed that all time scales of the investigated data carried nonlinear information.
Finally, inpainting assisted investigation of the time series turned out to be extremely powerful in removing spurious edge effects and in precisely localizing the passages

that exert most of the nonlinear influence. It further facilitates SRT based tests of highly symmetric time series.
Trajectories of particles from a simulation of turbulent dusty plasma supplied the last experimental analysis with acceleration time series. Time scale dependent phase anomalies could be verified in trajectories that traversed edge regions of the particle cloud, while no anomalies were detected for particles that followed stable movements.

Although the results presented so far do certainly not look too bad, this work hopefully just states some starting point in the field of Fourier phase based time series analysis. This thesis is largely restricted to the analysis to leptokurtic data (except for the examples in sections 5.6 and 5.9), which is of course only a tiny fraction of possible analysis subjects. Future work may allow for unwinding other types of phase entanglement, helping to better understand and utilizing Fourier phase information. This might not only be interesting from a theoretical point of view but also be of great value for financial applications, health sciences or even disaster prevention. In all of those fields new forecasting techniques are urgently required. Recent work even suggests promising development [Golestani and Gras, 2014; Birkholz et al., 2015], but is still based on computationally intense algorithms and neglects the very habitat of nonlinearities, that is, the Fourier phases.
In an often quoted article from 1999, Ivanov et al. have shown that measuring a decline in a multifractal measure can indicate life-threatening heart conditions, but they also uncovered that the *"nonlinear properties of the healthy heart rate are encoded in the Fourier phases"*. Let this be the motivation for further research on Fourier phases – on the *nonlinear heart* of time series.

Acknowledgements

First of all, I would like to thank my 2nd supervisor Dr. Christoph Räth for his outstanding scientific support during my Master's thesis, for his numerous and helpful advice and for steadily encouraging me to continue research on Fourier phases. Next, thanks to Dr. Hubertus Thomas, who enabled me to do my Master's thesis at his wonderful Research Group for Complex Plasma at the German Aerospace Center and to continue my work for an additional amount of time. I would like to also express my gratitude to Prof. Dr. Dr.h.c. Gregor Morfill for reviewing my thesis as my 1st supervisor.

Furthermore, I deeply appreciated the warm-hearted atmosphere among my colleges. Since my very first day at the research group, I received amazingly attentive and careful support by Dr. Daniel Mohr and Dr. Peter Huber with any hardware-, software-, or commonplace-issue I encountered. Daniel passionately assisted me with even sophisticated coding problems and always tried to pass on his knowledge to others. I further truly enjoyed stumbling into the interesting and arresting discussions with Peter that sooner or later were inevitably joined or left by Dr. Christina Knapek, Daniel or any other college.
Another special thank goes to Christina, for teaching me a lot about complex plasmas by showing me phenomena directly at the experimental setups and by supplying me with papers and books. Also for encouraging me to actually perform experiments, for enabling me to join the parabolic flight campaign and of course for the chilli seeds! Moreover, it was Christina and Daniel who offered to proof-read this manuscript and consequently drastically improved its quality. Thank you for this and everything else!
Another most pleasant factor was provided by my two office colleges Ingo Laut and Max Weber. Ingo always helped me with topics in data analysis or Python and the discussions with him not at least led to the idea of phase walk analysis. Max often drew my attention to some highly interesting programming tricks or techniques. Most importantly though, both of them ensured a very friendly and enjoyable atmosphere.
I would like to personally thank Alexander Böbel for all the nice discussions about physics we had and for being my *exercise sheet college* during Statistical Mechanics II. Without him, many sheets would certainly not have made it to the tutor's office.
Thanks as well to all the other members of the research group of course for providing such a sociable and professional scientific atmosphere.

Since this is the last and apparently most important artifact of my graduate studies, I do also have to thank my relatives, friends and former colleges. Especially my mother of course, who supported me in every respect and in any situation. Thank you for being there, whenever I need advice and for having done a presumably well and definitely heavy job in raising me.
I would like to thank my father for his financial support and likewise my dear first cousin once removed Markus. Thanks to all my friends for not taking me seriously in most situations but then again taking me seriously in some very rare situations. That is how you keep me alive.
Thanks to Dr. Wolfgang Wieser and Prof. Dr. Robert Huber for practicing non-stop quantitative thinking. Moreover, thank you Wolfgang for teaching me a whole lot about electronics, efficiency and hard work, and Robert for teaching me that no matter how hard you work, there is still some space left above. Both of them influenced my studies and lifestyle formatively. Thank you for that!
Finally, the additional proof-reader shall be mentioned: Franz. Thank you for your yellow.

This work has made use of data provided by the National Renewable Energy Laboratory ("NREL"), which is operated by the Alliance for Sustainable Energy, LLC ("ALLIANCE") for the U.S. Department Of Energy ("DOE") [National Renewable Energy Laboratory, 2014].

Appendix

Appendix A

Further Calculations

A.1 Proof of the Wiener-Khinchin-Theorem

$$\begin{aligned}
\mathcal{A}(\tau) = \int dt x^*(t)x(t+\tau) &= \int dt \int dk \int dk' \tilde{x}^*(k)\tilde{x}(k')e^{2\pi ikt}e^{-2\pi ik'(t+\tau)} \\
&= \int dk \int dk' \tilde{x}^*(k)\tilde{x}(k') \int dt e^{2\pi it(k-k')}e^{-2\pi ik'\tau} \\
&= \int dk \int dk' \tilde{x}^*(k)\tilde{x}(k')\delta(k-k')e^{-2\pi ik'\tau} \\
&= \int dk \tilde{x}^*(k)\tilde{x}(k)e^{-2\pi ik\tau} \\
&= \int dk \mathcal{P}(k)e^{-2\pi ik\tau}
\end{aligned}$$

A.2 No Correlation with White Power Spectra

Let us assume that the power spectrum of a time series $x(t)$ is white, that is, constant over all frequencies:

$$(P)(k) = \xi^2$$

It follows

$$\mathcal{A}(\tau) = \int dk \mathcal{P}(k)e^{-2\pi ik\tau} = \int dk \xi^2 e^{-2\pi ik\tau} = \xi^2\delta(\tau)$$

Hence, the autocorrelation functions is 0 everywhere except for $\tau = 0$.

A.3 Gaussian Probability Distribution

Maximizing the entropy of a PDF $f(x)$ with finite mean μ and variance σ^2 results in a normal distribution. To show this, one can use the method of Lagrange multipliers.

One has to maximize the entropy

$$S(f) = -\int dx f(x) \ln(f(x))$$

under following constraints

$$\int dx f(x) = 1$$
$$\int dx f(x) x = \mu$$
$$\int dx f(x)(x-\mu)^2 = \sigma^2.$$

The Lagrangian then becomes

$$\begin{aligned}\mathcal{L}(f,\alpha,\beta,\gamma) = \int dx \{ & -f(x)\ln(f(x)) \\ & + \alpha' \cdot [f(x) - 1] + \beta \cdot [f(x) \cdot x] \\ & + \gamma \cdot [f(x)(x-\mu)^2 - \sigma^2]\}.\end{aligned}$$

The functional derivative with respect to f is now set to 0:

$$\frac{\delta \mathcal{L}}{\delta f} = -\ln(f(x)) + \alpha + \beta x + \gamma(x-\mu)^2 = 0$$

(A 1 has implicitly be absorbed in a constant $\alpha = \alpha' - 1$.) Hence,

$$\begin{aligned}f(x) &= \exp(\gamma(x-\mu)^2 + \beta x + \alpha) = \exp(\alpha)\exp(\gamma(x-\mu)^2 + \beta x) \\ &= A\exp(\gamma(x-\mu)^2 + \beta x)\end{aligned}$$

To drastically shorten the algebraic derivation of the coefficients a symmetry argument can be applied. If the distribution is centered around $\mu = 0$, then it should be symmetric: $f(x|\mu = 0) = f(-x|\mu = 0)$. It follows that $\beta = 0$. Now the constraints are used to derive the coefficients:

$$\int dx A\exp(\gamma(x-\mu)^2) = A\sqrt{\frac{\pi}{-\gamma}} = 1 \Rightarrow A = \sqrt{\frac{-\gamma}{\pi}}$$

$$\int dx f(x)(x-\mu)^2 = \int dx A\exp(\gamma(x-\mu)^2)(x-\mu)^2 = \frac{-1}{2\gamma} = \sigma^2 \Rightarrow \gamma = \frac{-1}{2\sigma^2}$$

$$\Rightarrow f(x) = \frac{1}{\sqrt{2\pi}\sigma}\exp(\frac{-(x-\mu)^2}{2\sigma^2})$$

A.4 Maximum Entropy in Fourier Space

To see that a uniform phase distribution maximizes Entropy in Fourier space can also be shown with Lagrange multipliers. The Fourier representation is given by

$$\tilde{x}(k) = |x(k)| \exp(i\phi(k)).$$

Since the moduli $|x(k)|$ and the phases $\phi(k)$ are independent, the entropy can also be independently maximized for both. One applies the following two constraints:

$$\int d\phi f(\phi) = 1$$
$$\phi \in \{x \in \mathbb{R} | -\pi < x \leq \pi\}.$$

Hence,

$$\mathcal{L}(f, \alpha) = \int d\phi \{-f(\phi) \ln(f(\phi)) + \alpha \cdot [f(x) - 1]\}$$

and

$$\frac{\delta \mathcal{L}}{\delta f} = -\ln(f(\phi)) + \alpha - 1 = 0 \Rightarrow f(\phi) = \exp(\alpha - 1) = const..$$

Normalization by the first constraint further implies that

$$f(\phi) = \begin{cases} \frac{1}{2\pi} & \text{if } -\pi < \phi \leq \pi \\ 0 & \text{else} \end{cases}.$$

A.5 Variance of Random Walks

Let us consider a general random walk of the form

$$x_n = x_{n-1} + \Delta x$$

and assume that the steps Δx are independently and identically distributed with a finite mean μ and variance σ^2.
According to Tab. 2.1, the variance can in general be written as

$$\sigma_n^2 = \left\langle (x_n - \mu_n)^2 \right\rangle = \left\langle x_n^2 \right\rangle - \mu_n^2,$$

where the mean of the n^{th} step is given by

$$\mu_n = \langle x_{n-1} + \Delta x \rangle = \langle x_{n-1} \rangle + \langle \Delta x \rangle = \langle x_{n-1} \rangle + \mu$$

and hence,

$$\mu_n = n \cdot \mu.$$

For the remaining term, one can write

$$\begin{aligned}\left\langle x_n^2\right\rangle &= \left\langle (x_{n-1}+\Delta x)^2\right\rangle = \left\langle x_{n-1}^2\right\rangle + 2\left\langle x_{n-1}\Delta x\right\rangle + \left\langle \Delta x^2\right\rangle \\ &= \left\langle x_{n-1}^2\right\rangle + \left\langle \Delta x^2\right\rangle + 2\left\langle x_{n-1}\right\rangle\left\langle \Delta x\right\rangle = \left\langle x_{n-1}^2\right\rangle + \sigma^2 + \mu^2 + 2(n-1)\mu^2 \\ &= \left\langle x_{n-1}^2\right\rangle + \sigma^2 + (2n-1)\mu^2.\end{aligned}$$

The variance of the n^{th} step therefore becomes

$$\begin{aligned}\sigma_n^2 &= \left\langle x_n^2\right\rangle - \mu_n^2 = \left\langle x_{n-1}^2\right\rangle + \sigma^2 + (2n-1)\mu^2 - n^2\mu^2 = \left\langle x_{n-1}^2\right\rangle + \sigma^2 - (n-1)^2\mu^2 \\ &= \left\langle x_{n-1}^2\right\rangle - \mu_{(n-1)}^2 + \sigma^2 = \sigma_{n-1}^2 + \sigma^2.\end{aligned}$$

Thus, the variance scales linearly with n :

$$\sigma_n^2 = n \cdot \sigma^2.$$

Appendix B

Further Figures

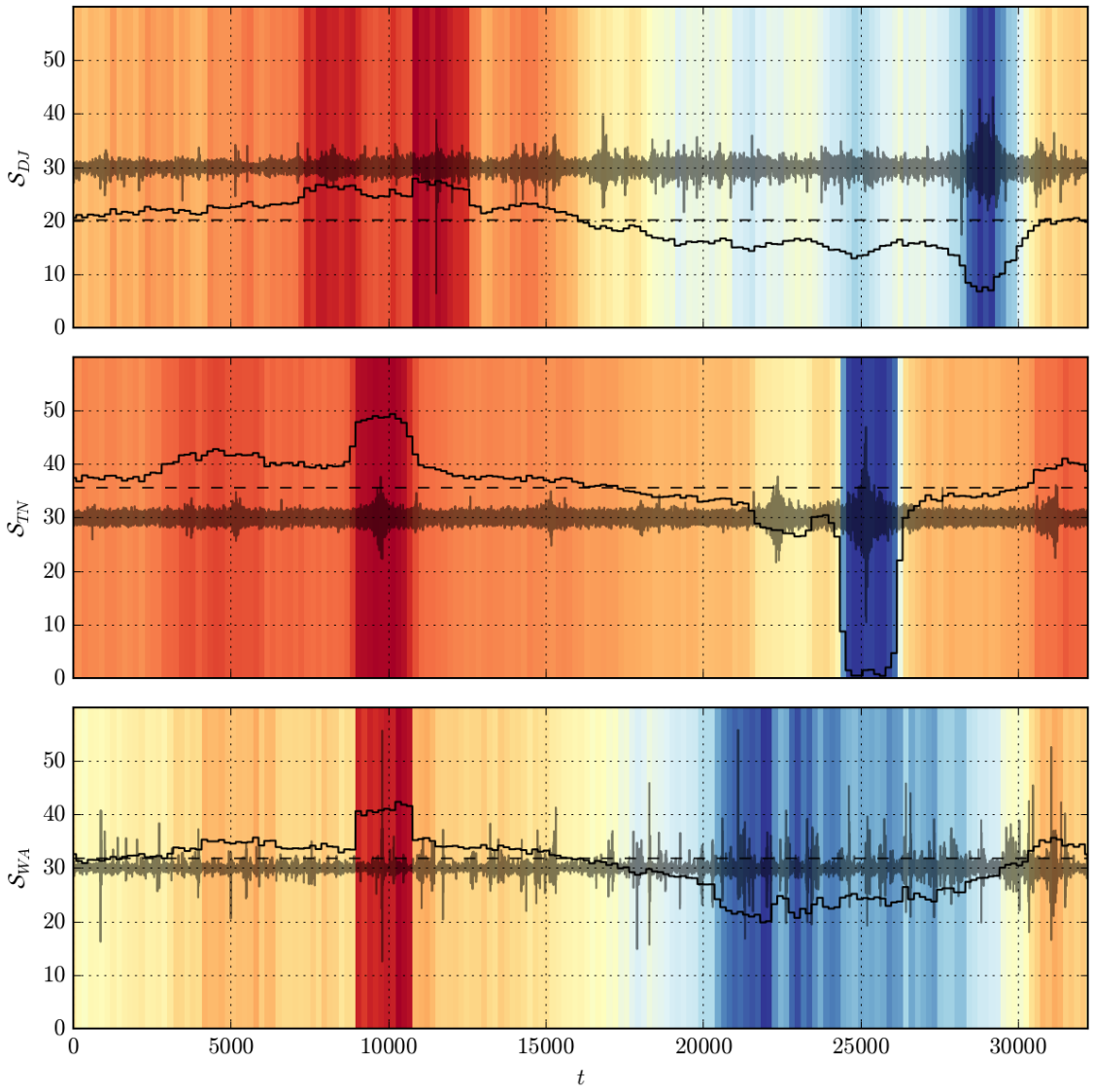

Figure B.1: SRT results for time series DJ, TN and WA with inpainted segments. The solid black curve in each graph shows the result $\mathcal{S}(\kappa = 16108)$ of the SRT-test of the time series when a region of width $= 1800$ at the corresponding position position t was replaced by a an inpainted segment. $\mathcal{S}(\kappa = 16108)$ of the unaltered time series is also indicated as dashed black lines. The background redundantly encodes this value: blue corresponds to a drop and red to an increase in $\mathcal{S}(\kappa)$. The grayish curves are the time series in arbitrary units. All time series have additionally be rotated by 180°. See Sec. 5.7 and Fig. 5.11 for further information.

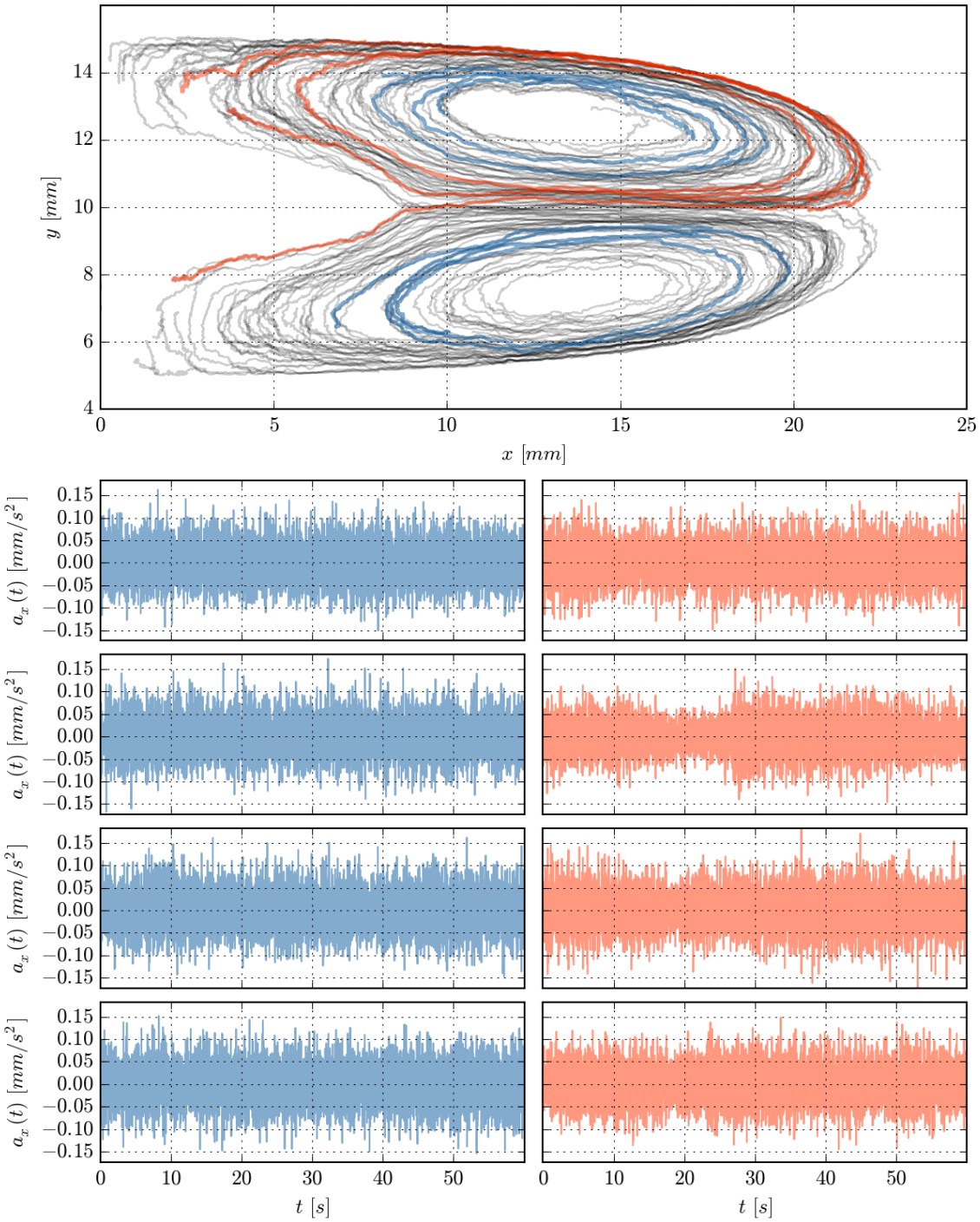

Figure B.2: Top: 100 randomly picked particle trajectories (gray) to visualize the system, four trajectories from the inner region of the vortices (blue) and four trajectories from regions near the void and / or the outer edges of the particle cloud (red). The left column below shows the acceleration in x-direction of the four stable oscillations (blue) and the right column the acceleration of the unstable trajectories (red). See Section 5.9 for further information.

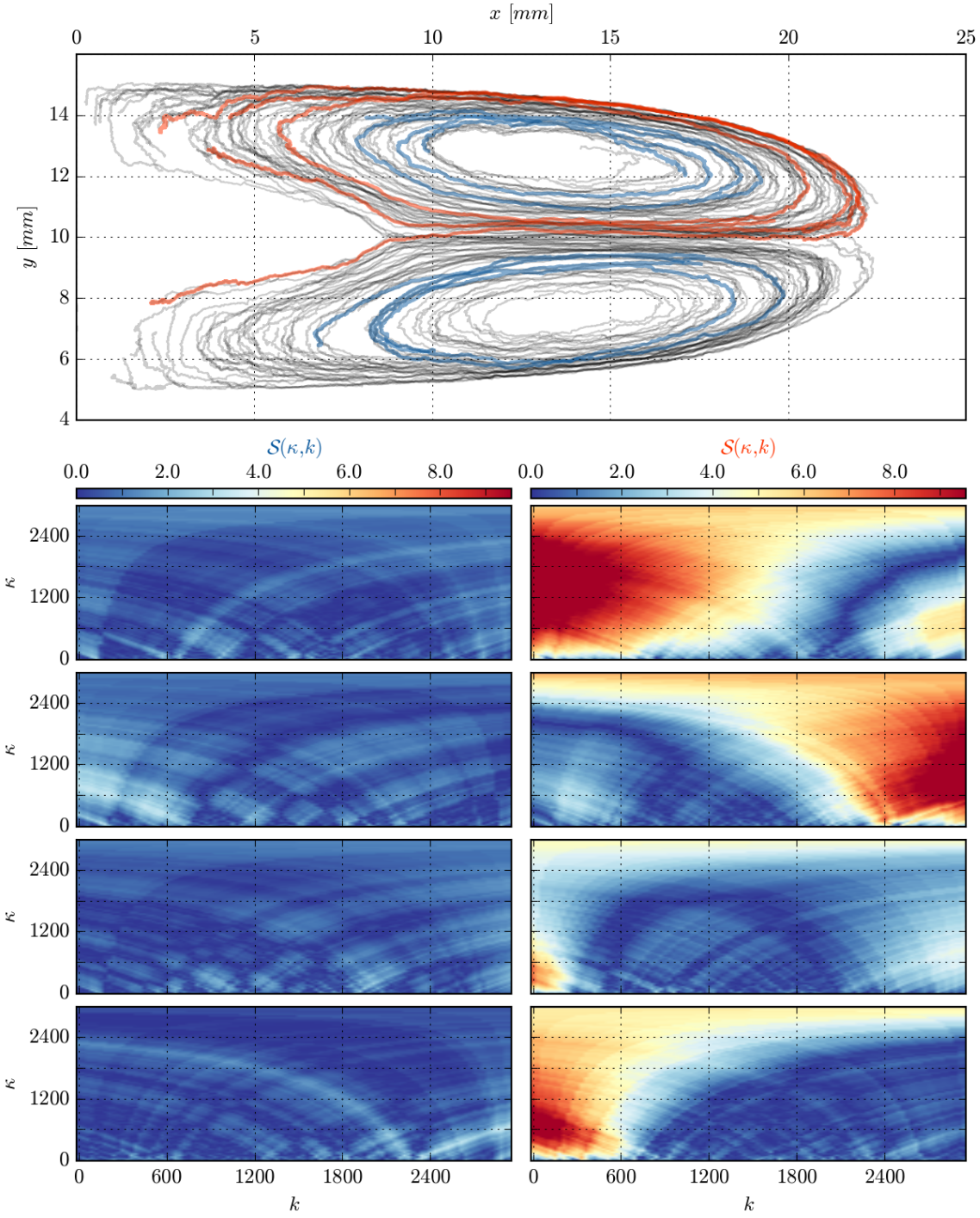

Figure B.3: Top: 100 randomly picked particle trajectories (gray) to visualize the system, four trajectories from the inner region of the vortices (blue) and four trajectories from regions near the void and / or the outer edges of the particle cloud (red). The latter show well-marked phase anomalies in the SRT results, while the stable vortex rotations are rather inconspicuous by tendency. Below: The left column shows the SR-maps that correspond to the the x-accelerations of the blue trajectories in the top figure and the right column those, corresponding to the red trajectories. Well observable, the stable rotations (blue, left) cause no significant deviations from the random walk hypothesis, while the outer trajectories (red, right) show large frequency dependent aberrations. See Section 5.9 for further information.

Bibliography

Altizer, S., Dobson, A., Hosseini, P., Hudson, P., Pascual, M., and Rohani, P. (2006). Seasonality and the dynamics of infectious diseases. *Ecology letters*, 9(4):467–484.

Alvarez-Ramirez, J., Cisneros, M., Ibarra-Valdez, C., and Soriano, A. (2002). Multifractal hurst analysis of crude oil prices. *Physica A: Statistical Mechanics and its Applications*, 313(3):651–670.

Andrzejak, R. G., Lehnertz, K., Mormann, F., Rieke, C., David, P., and Elger, C. E. (2001). Indications of nonlinear deterministic and finite-dimensional structures in time series of brain electrical activity: Dependence on recording region and brain state. *Physical Review E*, 64(6):061907.

Barlow, J. S. and Brown, R. M. (1955). An analog correlator system for brain potentials. *Technical Report*.

Bertalmio, M., Sapiro, G., Caselles, V., and Ballester, C. (2000). Image inpainting. In *Proceedings of the 27th annual conference on Computer graphics and interactive techniques*, pages 417–424. ACM Press/Addison-Wesley Publishing Co.

Birkholz, S., Brée, C., Demircan, A., and Steinmeyer, G. (2015). Predictability of rogue events. *Physical Review Letters*, 114(21):213901.

Box, G. E. and Jenkins, G. M. (1976). *Time series analysis: forecasting and control, revised ed*. Holden-Day.

Bylov, B., Vinograd, R., Grobman, D., and Nemytskii, V. (1966). The theory of lyapunov exponents.

Candès, E. J. and Donoho, D. L. (1999). Ridgelets: A key to higher-dimensional intermittency? *Philosophical Transactions of the Royal Society of London A: Mathematical, Physical and Engineering Sciences*, 357(1760):2495–2509.

Chiang, L.-Y. and Coles, P. (2000). Phase information and the evolution of cosmological density perturbations. *Monthly Notices of the Royal Astronomical Society*, 311(4):809–824.

Chiang, L.-Y., Coles, P., and Naselsky, P. (2002). Return mapping of phases and the analysis of the gravitational clustering hierarchy. *Monthly Notices of the Royal Astronomical Society*, 337(2):488–494.

Chiang, L.-Y., Naselsky, P. D., and Coles, P. (2007). Departure from gaussianity of the cosmic microwave background temperature anisotropies in the three-year wmap data. *The Astrophysical Journal*, 664(1):8.

Chiang, L.-Y., Naselsky, P. D., Verkhodanov, O. V., and Way, M. J. (2003). Non-gaussianity of the derived maps from the first-year wilkinson microwave anisotropy probe data. *The Astrophysical Journal Letters*, 590(2):L65.

Cochrane, J. H. (1988). How big is the random walk in gnp? *The Journal of Political Economy*, pages 893–920.

Coles, P. and Chiang, L.-Y. (2000). Characterizing the nonlinear growth of large-scale structure in the universe. *Nature*, 406(6794):376–378.

Coles, P., Dineen, P., Earl, J., and Wright, D. (2004). Phase correlations in cosmic microwave background temperature maps. *Monthly Notices of the Royal Astronomical Society*, 350(3):989–1004.

Cover, T. M. and Thomas, J. A. (1991). Entropy, relative entropy and mutual information. *Elements of Information Theory*, pages 12–49.

Dolan, K. T. and Spano, M. L. (2001). Surrogate for nonlinear time series analysis. *Physical Review E*, 64(4):046128.

Elad, M., Starck, J.-L., Querre, P., and Donoho, D. L. (2005). Simultaneous cartoon and texture image inpainting using morphological component analysis (mca). *Applied and Computational Harmonic Analysis*, 19(3):340–358.

Farmer, J. D. and Sidorowich, J. J. (1987). Predicting chaotic time series. *Physical review letters*, 59(8):845.

Feller, W. (1945). The fundamental limit theorems in probability. *Bulletin of the American Mathematical Society*, 51(11):800–832.

Fisher, R. A. et al. (1925). Applications of students distribution. *Metron*, 5(3):90–104.

Fortov, V. E., Ivlev, A., Khrapak, S., Khrapak, A., and Morfill, G. (2005). Complex (dusty) plasmas: Current status, open issues, perspectives. *Physics reports*, 421(1):1–103.

Frisch, U. (1995). *Turbulence: the legacy of AN Kolmogorov*. Cambridge university press.

Ghiglia, D. C. and Pritt, M. D. (1998). *Two-dimensional phase unwrapping: theory, algorithms, and software*. Wiley New York:.

Golestani, A. and Gras, R. (2014). Can we predict the unpredictable? *Scientific reports*, 4.

Grassberger, P. (1983). Generalized dimensions of strange attractors. *Physics Letters A*, 97(6):227–230.

Harris, F. J. (1978). On the use of windows for harmonic analysis with the discrete fourier transform. *Proceedings of the IEEE*, 66(1):51–83.

Heidemann, R., Zhdanov, S., Sütterlin, K., Thomas, H., and Morfill, G. (2011). Shear flow instability at the interface among two streams of a highly dissipative complex plasma. *EPL (Europhysics Letters)*, 96(1):15001.

Ho, K. K., Moody, G. B., Peng, C.-K., Mietus, J. E., Larson, M. G., Levy, D., and Goldberger, A. L. (1997). Predicting survival in heart failure case and control subjects by use of fully automated methods for deriving nonlinear and conventional indices of heart rate dynamics. *Circulation*, 96(3):842–848.

Hoyer, D., Schmidt, K., Bauer, R., Zwiener, U., Köhler, M., Lüthke, B., and Eiselt, M. (1997). Nonlinear analysis of heart rate and respiratory dynamics. *Engineering in Medicine and Biology Magazine, IEEE*, 16(1):31–39.

Itoh, K. (1982). Analysis of the phase unwrapping algorithm. *Applied Optics*, 21(14):2470–2470.

Ivanov, P. C., Amaral, L. A. N., Goldberger, A. L., Havlin, S., Rosenblum, M. G., Struzik, Z. R., and Stanley, H. E. (1999). Multifractality in human heartbeat dynamics. *Nature*, 399(6735):461–465.

Ivlev, A., Löwen, H., Morfill, G., and Royall, C. P. (2012). *Complex Plasmas and Colloidal Dispersions: Particle-Resolved Studies of Classical Liquids and Solids*. World Scientific.

Jenkinson, M. (2003). Fast, automated, n-dimensional phase-unwrapping algorithm. *Magnetic resonance in medicine*, 49(1):193–197.

Kantz, H. (1994). A robust method to estimate the maximal lyapunov exponent of a time series. *Physics letters A*, 185(1):77–87.

Kennel, M. B., Brown, R., and Abarbanel, H. D. (1992). Determining embedding dimension for phase-space reconstruction using a geometrical construction. *Physical review A*, 45(6):3403.

Kenney, F. and Keeping, E. (1951). *Mathematics of statistics-part two*. D. Van Nostrand Company, Inc Princeton,; New Jersey; Toronto; New York; London.

Knapek, C. A. (2011). *Phase transitions in two-dimensional complex plasmas*. Springer Science & Business Media.

Kolmogorov, A. N. (1941a). Dissipation of energy in locally isotropic turbulence. In *Dokl. Akad. Nauk SSSR*, volume 32,1, pages 16–18.

Kolmogorov, A. N. (1941b). The local structure of turbulence in incompressible viscous fluid for very large reynolds numbers. In *Dokl. Akad. Nauk SSSR*, volume 30,4, pages 299–303.

Kong, J., Hyde, T. W., Matthews, L., Qiao, K., Zhang, Z., and Douglass, A. (2011). One-dimensional vertical dust strings in a glass box. *Physical Review E*, 84(1):016411.

Kurths, J. and Herzel, H. (1987). An attractor in a solar time series. *Physica D: Nonlinear Phenomena*, 25(1):165–172.

LeBaron, B. (1994). Chaos and nonlinear forecastability in economics and finance. *Philosophical Transactions of the Royal Society of London A: Mathematical, Physical and Engineering Sciences*, 348(1688):397–404.

Lehnertz, K. and Elger, C. E. (1998). Can epileptic seizures be predicted? evidence from nonlinear time series analysis of brain electrical activity. *Physical Review Letters*, 80(22):5019.

Lo, A. W. and MacKinlay, A. C. (1988). Stock market prices do not follow random walks: Evidence from a simple specification test. *Review of financial studies*, 1(1):41–66.

Lyapunov, A. M. (1892). The general problem of motion stability. *Annals of Mathematics Studies*, 17.

Lyapunov, A. M. (1992). The general problem of the stability of motion. *International Journal of Control*, 55(3):531–534.

Mallat, S. G. (1989). A theory for multiresolution signal decomposition: the wavelet representation. *Pattern Analysis and Machine Intelligence, IEEE Transactions on*, 11(7):674–693.

Merlino, R., Barkan, A., Thompson, C., and Dangelo, N. (1998). Laboratory studies of waves and instabilities in dusty plasmas. *Physics of Plasmas (1994-present)*, 5(5):1607–1614.

Modest, H., Räth, C., Banday, A., Górski, K., and Morfill, G. (2014). Correlating fourier phase information with real-space higher order statistics in cmb data. *Physical Review D*, 89(12):123004.

Morfill, G. E., Rubin-Zuzic, M., Rothermel, H., Ivlev, A. V., Klumov, B. A., Thomas, H. M., Konopka, U., and Steinberg, V. (2004). Highly resolved fluid flows:liquid plasmas at the kinetic level. *Physical review letters*, 92(17):175004.

National Renewable Energy Laboratory, . (2014). National renewable energy laboratory. [`http://www.nrel.gov/electricity/transmission/eastern_wind_dataset.html`; accessed 19-September-2014].

Nefedov, A. P., Morfill, G. E., Fortov, V. E., Thomas, H. M., Rothermel, H., Hagl, T., Ivlev, A. V., Zuzic, M., Klumov, B. A., Lipaev, A. M., et al. (2003). Pke-nefedov: plasma crystal experiments on the international space station. *New Journal of Physics*, 5(1):33.

Nosenko, V., Goree, J., Ma, Z., and Piel, A. (2002). Observation of shear-wave mach cones in a 2d dusty-plasma crystal. *Physical review letters*, 88(13):135001.

Nyquist, H. (1928). Certain topics in telegraph transmission theory. *American Institute of Electrical Engineers, Transactions of the*, 47(2):617–644.

Otnes, R. K. (2008). Notes on mechanical fourier analyzers. *J. Oughtred Soc*, 17:34–41.

Packard, N. H., Crutchfield, J. P., Farmer, J. D., and Shaw, R. S. (1980). Geometry from a time series. *Physical review letters*, 45(9):712.

Pascual, M., Rodó, X., Ellner, S. P., Colwell, R., and Bouma, M. J. (2000). Cholera dynamics and el nino-southern oscillation. *Science*, 289(5485):1766–1769.

Pearson, K. (1905). The problem of the random walk. *Nature*, 72(1865):294.

Pearson, K. (1916). Mathematical contributions to the theory of evolution. xix. second supplement to a memoir on skew variation. *Philosophical Transactions of the Royal Society of London. Series A, Containing Papers of a Mathematical or Physical Character*, pages 429–457.

Phillips, M. (2010). Nasdaq: Heres our timeline of the flash crash. [`http://blogs.wsj.com/marketbeat/2010/05/11/nasdaq-heres-our-timeline-of-the-flash-crash/`; accessed 05-September-2015].

Pires, S., Starck, J.-L., Amara, A., Teyssier, R., Réfrégier, A., and Fadili, J. (2009). Fast statistics for weak lensing (fastlens): fast method for weak lensing statistics and map making. *Monthly Notices of the Royal Astronomical Society*, 395(3):1265–1279.

Pólya, G. (1920). Über den zentralen grenzwertsatz der wahrscheinlichkeitsrechnung und das momentenproblem. *Mathematische Zeitschrift*, 8(3):171–181.

Ragwitz, M. and Kantz, H. (2000). Detecting non-linear structure and predicting turbulent gusts in surface wind velocities. *EPL (Europhysics Letters)*, 51(6):595.

Räth, C., Gliozzi, M., Papadakis, I., and Brinkmann, W. (2012). Revisiting algorithms for generating surrogate time series. *Physical review letters*, 109(14):144101.

Räth, C. and Laut, I. (2015). Time series with tailored nonlinearities. *arXiv preprint arXiv:1509.00223*.

Rényi, A. (1961). On measures of entropy and information. In *Proceedings of the Fourth Berkeley Symposium on Mathematical Statistics and Probability, Volume 1: Contributions to the Theory of Statistics*. The Regents of the University of California.

Richman, J. S. and Moorman, J. R. (2000). Physiological time-series analysis using approximate entropy and sample entropy. *American Journal of Physiology-Heart and Circulatory Physiology*, 278(6):H2039–H2049.

Sato, K., Garcia, R., Pires, S., Ballot, J., Mathur, S., Mosser, B., Rodriguez, E., Starck, J., and Uytterhoeven, K. (2010). Inpainting: a powerful interpolation technique for helio-and asteroseismic data. *arXiv preprint arXiv:1003.5178*.

Schreiber, T. (1998). Constrained randomization of time series data. *Physical Review Letters*, 80(10):2105.

Schreiber, T. and Schmitz, A. (1996). Improved surrogate data for nonlinearity tests. *Physical Review Letters*, 77(4):635.

Schreiber, T. and Schmitz, A. (1997). Discrimination power of measures for nonlinearity in a time series. *Physical Review E*, 55(5):5443.

Schreiber, T. and Schmitz, A. (2000). Surrogate time series. *Physica D: Nonlinear Phenomena*, 142(3):346–382.

Schwabe, M., Zhdanov, S., Räth, C., Graves, D. B., Thomas, H. M., and Morfill, G. E. (2014). Collective effects in vortex movements in complex plasmas. *Physical review letters*, 112(11):115002.

Shannon, C. (1948). A mathematical theory of communication. *Bell System Technical Journal, The*, 27(3):379–423.

Small, M. and Tse, C. K. (2003). Determinism in financial time series. *Studies in nonlinear dynamics & Econometrics*, 7(3).

Stannard, A. and Coles, P. (2005). Random-walk statistics and the spherical harmonic representation of cosmic microwave background maps. *Monthly Notices of the Royal Astronomical Society*, 364(3):929–933.

Starck, J.-L., Murtagh, F., Candes, E. J., and Donoho, D. L. (2003). Gray and color image contrast enhancement by the curvelet transform. *Image Processing, IEEE Transactions on*, 12(6):706–717.

Strozzi, F., Zaldıvar, J.-M., and Zbilut, J. P. (2002). Application of nonlinear time series analysis techniques to high-frequency currency exchange data. *Physica A: Statistical Mechanics and its Applications*, 312(3):520–538.

Student (1908). The probable error of a mean. *Biometrika*, pages 1–25.

Sugihara, G. and May, R. M. (1990). Nonlinear forecasting as a way of distinguishing chaos from measurement error in time series. *Nature*, 344:734–741.

Sung, R., Short, J., and Coles, P. (2010). Statistical characterization of temperature patterns in anisotropic cosmologies. *arXiv preprint arXiv:1004.1925*.

Takens, F. (1981). *Detecting strange attractors in turbulence*. Springer.

Theiler, J., Eubank, S., Longtin, A., Galdrikian, B., and Doyne Farmer, J. (1992). Testing for nonlinearity in time series: the method of surrogate data. *Physica D: Nonlinear Phenomena*, 58(1):77–94.

Thomas, H., Morfill, G., Demmel, V., Goree, J., Feuerbacher, B., and Möhlmann, D. (1994). Plasma crystal: Coulomb crystallization in a dusty plasma. *Physical Review Letters*, 73(5):652.

Thomas, H., Morfill, G., Fortov, V., Ivlev, A., Molotkov, V., Lipaev, A., Hagl, T., Rothermel, H., Khrapak, S., Suetterlin, R., et al. (2008). Complex plasma laboratory pk-3 plus on the international space station. *New journal of physics*, 10(3):033036.

Thomas, H. M. and Morfill, G. E. (1996). Melting dynamics of a plasma crystal. *Nature*.

Vautard, R. and Ghil, M. (1989). Singular spectrum analysis in nonlinear dynamics, with applications to paleoclimatic time series. *Physica D: Nonlinear Phenomena*, 35(3):395–424.

Vio, R., Cristiani, S., Lessi, O., and Provenzale, A. (1992). Time series analysis in astronomy-an application to quasar variability studies. *The Astrophysical Journal*, 391:518–530.

Walker, G. (1931). On periodicity in series of related terms. *Proceedings of the Royal Society of London. Series A, Containing Papers of a Mathematical and Physical Character*, pages 518–532.

Whitle, P. (1951). *Hypothesis testing in time series analysis*, volume 4. Almqvist & Wiksells.

Wiener, N. (1923). Differential space. *Journal of Mathematical Physics*, 2:131–174.

Wiener, N. (1930). Generalized harmonic analysis. *Acta mathematica*, 55(1):117–258.

Wiener, N. (1961). *Cybernetics or Control and Communication in the Animal and the Machine*, volume 25. MIT press.

Wikipedia (2015). Spectral density — wikipedia, the free encyclopedia. [`https://en.wikipedia.org/wiki/Spectral_density`; accessed 20-September-2015].

Williamson, S. H. (2015). Daily closing value of the dow jones average, 1885 to present. MeasuringWorth.

Wörner, L., Räth, C., Nosenko, V., Zhdanov, S., Thomas, H., Morfill, G., Schablinski, J., and Block, D. (2012). String structures in driven 3d complex-plasma clusters. *EPL (Europhysics Letters)*, 100(3):35001.

Wu, M.-C. (2007a). Phase correlation of foreign exchange time series. *Physica A: Statistical Mechanics and its Applications*, 375(2):633–642.

Wu, M.-C. (2007b). Phase statistics approach to physiological and financial time series. *AAPPS Bulletin*, 17(2):21.

Yule, G. U. (1927). On a method of investigating periodicities in disturbed series, with special reference to wolfer's sunspot numbers. *Philosophical Transactions of the Royal Society of London. Series A, Containing Papers of a Mathematical or Physical Character*, pages 267–298.

Erklärung

Hiermit erkläre ich, die vorliegende Arbeit selbständig verfasst zu haben und keine anderen als die in der Arbeit angegebenen Quellen und Hilfsmittel benutzt zu haben.

_____
Ort, Datum

_____
Unterschrift